Draft version January 2, 2023
Typeset using LaTeX **twocolumn** style in AASTeX631

arXiv:2209.12224v2 [astro-ph.SR] 30 Dec 2022

Chemo-Dynamically Tagged Groups of CEMP Stars in the Halo of the Milky Way. I. Untangling the Origins of CEMP-*s* and CEMP-no Stars

Joseph Zepeda [1,2] Timothy C. Beers [1,2] Vinicius M. Placco [3] Derek Shank [1,2] Dmitrii Gudin [4] Yutaka Hirai [1,5,2,*] Mohammad Mardini,[6,7] Colin Pifer,[1,2] Thomas Catapano,[1,2] and Sean Calagna[1,2]

[1] *Department of Physics and Astronomy, University of Notre Dame, Notre Dame, IN 46556, USA*
[2] *Joint Institute for Nuclear Astrophysics – Center for the Evolution of the Elements (JINA-CEE), USA*
[3] *NSF's NOIRLab, 950 N. Cherry Ave., Tucson, AZ 85719, USA*
[4] *Department of Mathematics, University of Maryland, College Park, MD 20742-4015 USA*
[5] *Astronomical Institute, Tohoku University, 6-3 Aoba, Aramaki, Aoba-ku, Sendai, Miyagi 980-8578, Japan*
[6] *Kavli IPMU (WPI), UTIAS, The University of Tokyo, Kashiwa, Chiba 277-8583, Japan*
[7] *Institute for AI and Beyond, The University of Tokyo 7-3-1 Hongo, Bunkyo-ku, Tokyo 113-8655, Japan*

ABSTRACT

We construct a sample of 644 carbon-enhanced metal-poor (CEMP) stars with abundance analyses based on moderate- to high-resolution spectroscopic studies. Dynamical parameters for these stars are estimated, based on radial velocities, Bayesian parallax-based distance estimates, and proper motions from *Gaia* EDR3 and DR3, supplemented by additional available information where needed. After separating our sample into the different CEMP morphological groups in the Yoon-Beers Diagram of absolute carbon abundance vs. metallicity, we used the derived specific energies and actions (E, J_r, J_ϕ, J_z) to cluster them into Chemo-Dynamically Tagged Groups (CDTGs). We then analyzed the elemental-abundance dispersions within these clusters by comparing them to the dispersion of clusters that were generated at random. We find that, for the Group I (primarily CEMP-*s* and CEMP-*r*/*s*) clustered stars, there exist statistically insignificant intra-cluster dispersions in [Fe/H], $[C/Fe]_c$ (evolution corrected carbon), and [Mg/Fe] when compared to the intra-cluster dispersions of randomly clustered Group I CEMP stars. In contrast, the Group II (primarily CEMP-no) stars exhibit clear similarities in their intra-cluster abundances, with very low, statistically significant, dispersions in $[C/Fe]_c$. and marginally significant results in [Mg/Fe]. These results strongly indicate that Group I CEMP stars received their carbon enhancements from local phenomena, such as mass transfer from a evolved binary companion in regions with extended star-formation histories, while the CDTGs of Group II CEMP stars formed in low-metallicity environments that had already been enriched in carbon, likely from massive rapidly rotating ultra and hyper metal-poor stars and/or supernovae associated with high-mass early generation stars.

Keywords: galaxies: dwarf — Galaxy: halo — stars: kinematics and dynamics — stars: abundances — stars: Population II — stars: carbon-enhanced

1. INTRODUCTION

The nature of the first generation of stars in the Universe, the so-called Population III (Pop III) stars, is of primary interest in Stellar and Galactic Archaeology. These stars are thought to have been massive and short-lived (Bromm et al. 1999; Omukai et al. 2005). Detailed models of rapidly rotating, ultra metal-poor (UMP; [Fe/H] < -4.0) and hyper metal-poor (HMP; [Fe/H] < -5.0) Pop III stars (e.g., Meynet et al. 2006, 2010; Maeder & Meynet 2015; Hirano et al. 2015), as well as the so-called faint (mixing and fallback) supernovae models (e.g., Umeda & Nomoto 2005; Nomoto et al. 2013; Tominaga et al. 2014), which can apply to somewhat higher metallicities, such as extremely metal-poor (EMP; [Fe/H] < -3.0) stars, produce prodigious amounts of CNO, capable of enriching the natal gas from which later generations of presently observed, long-lived, low-mass stars are formed. The initial mass function (IMF) of Pop III stars and the nucleosynthesis path-

* JSPS Research Fellow

ways involved in their production of the elements incorporated into lower-mass next-generation (Pop II) stars can thus be constrained from studies of carbon-enhanced metal-poor (CEMP) stars, providing essential information on early Galactic chemical evolution and on the nature of the very first stars.

Carbon can be also produced in significant amounts by low-mass ($M < 1 - 3M_{\odot}$) stars in their asymptotic giant branch (AGB) stage of evolution (e.g., Suda et al. 2004; Herwig 2005; Lucatello et al. 2005; Bisterzo et al. 2011; Starkenburg et al. 2014; Hansen et al. 2015). If such a star is a member of a binary (or multiple) system, the transfer of mass to a companion star via Roche lobe overflow (or more likely winds) allows the nucleosynthetic products of the donor (the erstwhile primary star) to be preserved on the surface of the receiving star (Stancliffe et al. 2007; Abate et al. 2015). If the receiving star has a mass $M \lesssim 0.7M_{\odot}$, its lifetime exceeds the Hubble time, and can be observed today.

The first spectroscopic surveys to assemble significantly large samples of very metal-poor (VMP; [Fe/H] < -2.0) Pop II stars in the halo of the Milky Way (MW) were the HK (Beers et al. 1985, 1992) and Hamburg/ESO (Christlieb 2003) objective-prism surveys. Beers & Christlieb (2005) provided the basis for the modern nomenclature for describing stars of various (low) metallicities, and suggested initial classifications, based on their carbon and neutron-capture element abundances. Of particular interest to the present study are the various classes of CEMP stars, distinguished by their high level of carbonicity, [C/Fe] (originally set at [C/Fe] $> +1.0$, now usually taken to be [C/Fe] $> +0.7$).

Subsequent surveys have greatly enlarged the numbers of recognized CEMP stars to many thousands, including the Sloan Digital Sky Survey (York et al. 2000) and its extensions (SEGUE, Yanny et al. 2009; SEGUE-2, Rockosi et al. 2022), AEGIS (Keller et al. 2007), LAMOST (Deng et al. 2012), and Pristine (Starkenburg et al. 2017).

CEMP stars have been demonstrated to increase in frequency with decreasing metallicity. They comprise approximately 30% of all stars with [Fe/H] < -2.0, 60% for [Fe/H] < -3.0, 80% for [Fe/H] < -3.5, and approaching 100% (see Caffau et al. (2011) for a possible exception) for [Fe/H] < -4.0 (see Figure 6 of Yoon et al. 2018). This fundamental result indicates that the most metal-poor CEMP stars may preserve the chemical-abundance signature of the very first generations of stars, making them extremely valuable for the purposes of Stellar and Galactic Archaeology (Frebel & Norris 2015).

Table 1. CEMP Sub-class Definitions

Sub-classes	Definition
CEMP	[C/Fe] $> +0.7$
CEMP-r	[C/Fe] $> +0.7$, [Eu/Fe] $> +0.7$, [Ba/Eu] < 0.0
CEMP-s	[C/Fe] $> +0.7$, [Ba/Fe] $> +1.0$, [Ba/Eu] $> +0.5$
CEMP-i (r/s)	[C/Fe] $> +0.7$, $0.0 <$ [Ba/Eu] $< +0.5$ or
	[C/Fe] $> +0.7$, $0.0 \leq$ [La/Eu] $\leq +0.6$
CEMP-no	[C/Fe] $> +0.7$, [Ba/Fe] < 0.0

CEMP stars can be divided into multiple sub-classes. Work subsequent to the original Beers & Christlieb (2005) classification has introduced a number of refinements; we refer the interested reader to the review by Frebel (2018). In the present work, we adopt the classifications listed in Table 1. The primary sub-classes of interest in this paper are the CEMP-s stars, which exhibit over-abundances of neutron-capture elements ([Ba/Fe] $> +1.0$, [Ba/Eu] $> +0.5$) associated with production by the s-process, and the CEMP-no stars, which exhibit no enhancements of neutron-capture elements ([Ba/Fe] < 0.0)

It has also been demonstrated that the frequencies of CEMP-s and CEMP-no stars are not the same in different regions (and populations) of the MW. Specifically, CEMP-s stars are primarily associated with the Metal-Weak Thick Disk (MWTD) and inner-halo regions, while the bulk of the CEMP-no stars are found in the outer-halo region (Carollo et al. 2012, 2014; Lee et al. 2017; Yoon et al. 2018; Lee et al. 2019). These, and other authors, have pointed to this evidence as supporting differences in the formation and accretion histories of the various Galactic stellar populations.

Rossi et al. (2005) first pointed out that CEMP stars might not share a single nucleosynthetic origin, based on the apparent bimodal distribution of [C/Fe] and absolute carbon abundance, A(C)[1], at low metallicity (see their Figure 12). Later, Spite et al. (2013) and Bonifacio et al. (2015) presented evidence that there existed high and low "bands" in plots of A(C) vs. [Fe/H] for main-sequence turnoff stars and mildly evolved subgiants, primarily associated with CEMP-s and CEMP-no stars, respectively.

[1] $A(\mathrm{C}) = \log \epsilon(\mathrm{C}) = \log(\mathrm{N_C}/\mathrm{N_H}) + 12$, where $\mathrm{N_C}$ and $\mathrm{N_H}$ represent the number densities of carbon and hydrogen, respectively. A(C) is interchangeably used as [C/H] + $A(\mathrm{C})_{\odot}$, where $A(\mathrm{C})_{\odot}$ is the absolute Solar carbon abundance.

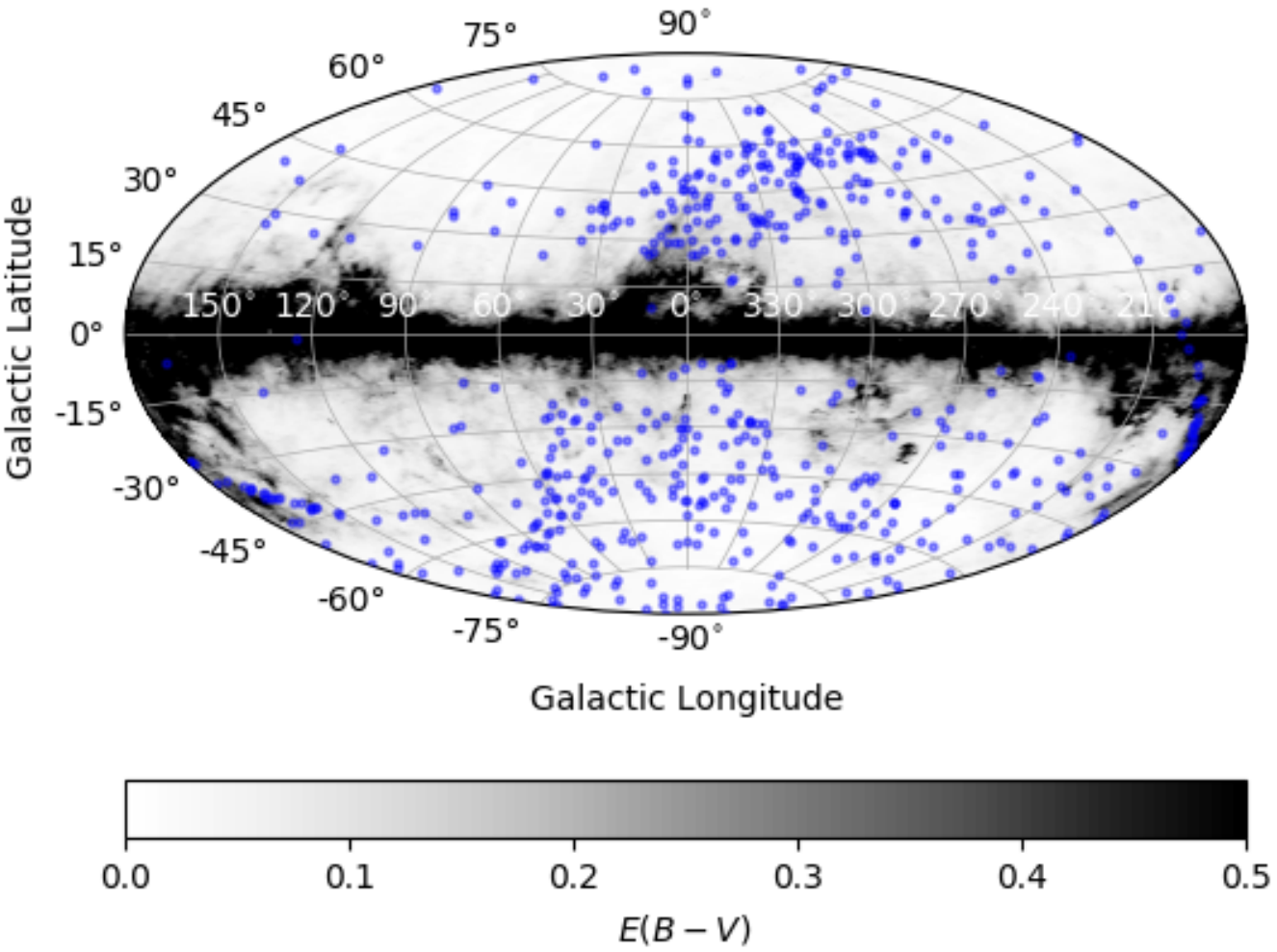


Figure 1. Spatial distribution of the Initial Sample of CEMP stars. The Galactic reddening map is taken from Schlegel et al. (1998) and recalibrated by Schlafly & Finkbeiner (2011), shown as the background on a gray scale with darker regions corresponding to greater reddening.

The full richness of the behavior of CEMP stars in the A(C)-[Fe/H] space was revealed in Figure 1 of Yoon et al. (2016) – the so-called Yoon-Beers Diagram, which separated CEMP stars into three morphological groups. Yoon et al. identified the great majority of CEMP-s stars as CEMP Group I stars, based on their distinctively higher A(C) compared to the CEMP-no stars, while most CEMP-no stars were classified as either CEMP Group II or Group III stars. The Group II stars exhibit a strong dependency of A(C) on [Fe/H], while the Group III stars show no such dependency. Based on this, and the clear differences between Group II and Group III stars in the A(Na)-A(C) and A(Mg)-A(C) spaces (Figure 4 of Yoon et al.), these authors argued for the existence of multiple progenitors and/or environments in which the CEMP-no stars formed.

Examination of the effects of dust cooling for varied compositions (e.g., carbon- vs. silicate-based dust grains), could account for the formation of both the Group II and III CEMP-no stars (see, e.g., Chiaki et al. 2017). Simulations of Pop III star enrichment by Sarmento et al. (2016) exhibited patterns in the A(C)-[Fe/H] space that can be associated with these same Groups (see their Figure 13). Simulations of Pop II star formation by Sharma et al. (2018b) show different formation pathways for Group I and Group II CEMP stars. It should be noted that Yoon et al. (2016) also pointed out that some CEMP stars exhibited anomalous abundance patterns within these different groups, such as stars with $A(C)_c < 7.1$ while [Ba/Fe] > 0.0 or $A(C)_c > 7.1$ while [Ba/Fe] $< +1.0$. Since the causes of these abundance patterns are not yet understood, their relative numbers are low compared to CEMP stars as a whole, and not all of the CEMP stars have the abundance measurements required to determine their anoma-

Table 2. Identified CEMP stars and their Group Associations

Name	Group	T_{eff} (K)	log g	[Fe/H]	$[C/Fe]_c$	$A(C)_c$	[Mg/Fe]	[Sr/Fe]	[Y/Fe]	[Ba/Fe]	[Eu/Fe]
HD 224959	I	5050	2.100	−2.42	+2.04	8.05	+0.39	+1.50	...	+2.07	+2.01
SDSS J000219.87+292851.8	I	6150	4.000	−3.26	+2.63	7.80	+0.36	+0.27	...	+1.83	...
BPS CS 29503−0010	I	6050	3.660	−1.70	+1.65	8.38	...	+1.13	...	+1.81	+1.69
HE 0002−1037	I	4673	1.280	−3.75	+3.43	8.11	...	...	...	...	...
BPS CS 31070−0073*	I/II	6190	3.860	−2.55	+1.34	7.22	+0.53	+1.75	...	+2.28	+2.74
HE 0007−1832	I	6500	3.800	−2.79	+2.79	8.43	+0.55	+0.08	...	+0.04	¡+1.70
HE 0010−3422	I	5400	3.100	−2.78	+1.93	7.58	+0.34	+0.77	...	+1.46	+1.64
HE 0012−1441	I	5750	3.500	−2.52	+1.71	7.62	+0.83	...	...	+1.10	...
HE 0013−0257	II	4500	0.500	−3.82	+0.93	5.54	+0.68	−0.46	...	−1.16	¡+0.67
HE 0015+0048	II	4600	0.900	−3.07	+1.27	6.63	+0.65	−1.07	...	−1.18	¡+0.75
HE 0017−4346	I	6198	3.800	−3.07	+3.02	8.38	+0.86	+0.84	...	+1.23	¡+0.99
HE 0017+0055	I	4261	0.800	−2.47	+2.80	8.76	...	...	...	+2.30	+2.14
SMSS J002148.06−471132.1	II	4765	1.400	−3.17	+0.78	6.04	+0.43	+0.02	...	−1.18	¡+0.50
2MASS J00224486−1724290*	II	4765	1.550	−4.05	+2.07	6.45	+1.03	−0.73	...	−1.10	+0.25
SDSS J002314.00+030758.0*	III	5997	4.600	−5.80	+3.76	6.39	+3.33	...	...	...	...
HE 0024−2523	I	6625	4.300	−2.72	+2.69	8.40	+0.71	+0.44	...	+1.41	¡+0.07
BPS CS 22882−0012	I/II	6290	3.800	−2.75	+1.10	6.78	+0.36	+0.56	...	+0.61	¡+1.23
BPS CS 31062−0050	I	5600	3.000	−2.32	+2.12	8.23	+0.59	+0.96	...	+2.35	+1.87
2MASS J00305267−1007042	I/II	4831	1.480	−2.35	+0.88	6.96	+0.24	+0.50	...	−0.71	+0.00
SDSS J003602.17−104336.2	I	6500	4.500	−2.50	+2.37	8.30	+0.27	−0.13	...	+0.37	...
RAVE J003946.9−684957	II	4631	1.160	−2.62	+0.73	6.54	...	+0.43	...	−0.10	−0.38
BPS CS 29497−0030	I	7000	4.000	−2.52	+2.37	8.28	+0.35	+1.30	...	+2.75	+1.71
BPS CS 29497−0034	I	4800	1.800	−2.90	+2.78	8.31	+0.70	+1.05	...	+1.98	+1.79
G 270−51	I	6000	3.800	−2.74	+2.39	8.08	+0.43	+0.18	...	+1.96	+1.39
2MASS J00453930−7457294	I	4947	2.010	−2.00	+0.99	7.42	...	+0.83	...	+0.37	+0.55

NOTE—This table is a stub; the full table is available in the electronic edition. Stars with names that end with * are not in the Final Sample.

lous status, we make no distinctions of these stars in this work.

In light of the above, it is likely that at least some classes of CEMP stars (notably, CEMP-no stars, but also some CEMP-*s* stars) were not formed in-situ in the Milky Way, but, rather, were born in low- and intermediate-mass satellite dwarf galaxies that were later accreted into it. According to early simulations (e.g., Helmi & de Zeeuw 2000), and many since, a large fraction (at least 50%) of Galactic accretion events can be recovered by applying clustering algorithms to the phase space of energies and other dynamical parameters of individual field stars. This opens the possibility of using a clustering approach to match CEMP stars formed in similar environments with each other by identifying them as members of individual Chemo-Dynamically Tagged Groups (CDTGs), which we pursue in this paper.

A pilot effort illustrating the application of this approach to chemically peculiar stars in the halo of the MW was conducted by Roederer et al. (2018), specific to *r*-process-enhanced stars, based on a relatively small sample size of 35 such stars. The sample was expanded considerably (426 *r*-process-enhanced stars) by Gudin et al. (2021), who demonstrated clear evidence that *r*-process-enhanced stars shared common chemical-evolution histories, presumably in their parent dwarf galaxies. Shank et al. (2022a) analyzes a sample of $\sim$ 1700 *r*-process-enhanced stars, reaching similar conclusions.

Another recent work, (Yuan et al. 2020), explored the clustering of a large data set of VMP MW halo stars. Through application of a trained neural network (STARGO), these authors successfully mapped dynamically tagged groups (DTGs) of VMP stars onto known more-massive sub-structures in the MW, and identified new DTGs for future spectroscopic follow-up. Other recent examples of this approach include an analysis of HK/HES stars (Limberg et al. 2021), the Best and Brightest survey (Shank et al. 2022b), and stars from the RAVE survey (Shank et al. 2022).

In this work, we derive dynamical parameters for a sample of 572 (of an initial sample of 644) CEMP stars with available moderate- to high-resolution spectroscopy ($R \geq 4350$).

This paper is outlined as follows. Section 2 describes the assembly of this sample, along with the adopted distance estimates, radial velocities, proper motions, and the subset of chemical abundances we consider. We also briefly describe the nature of this sample in this sec-

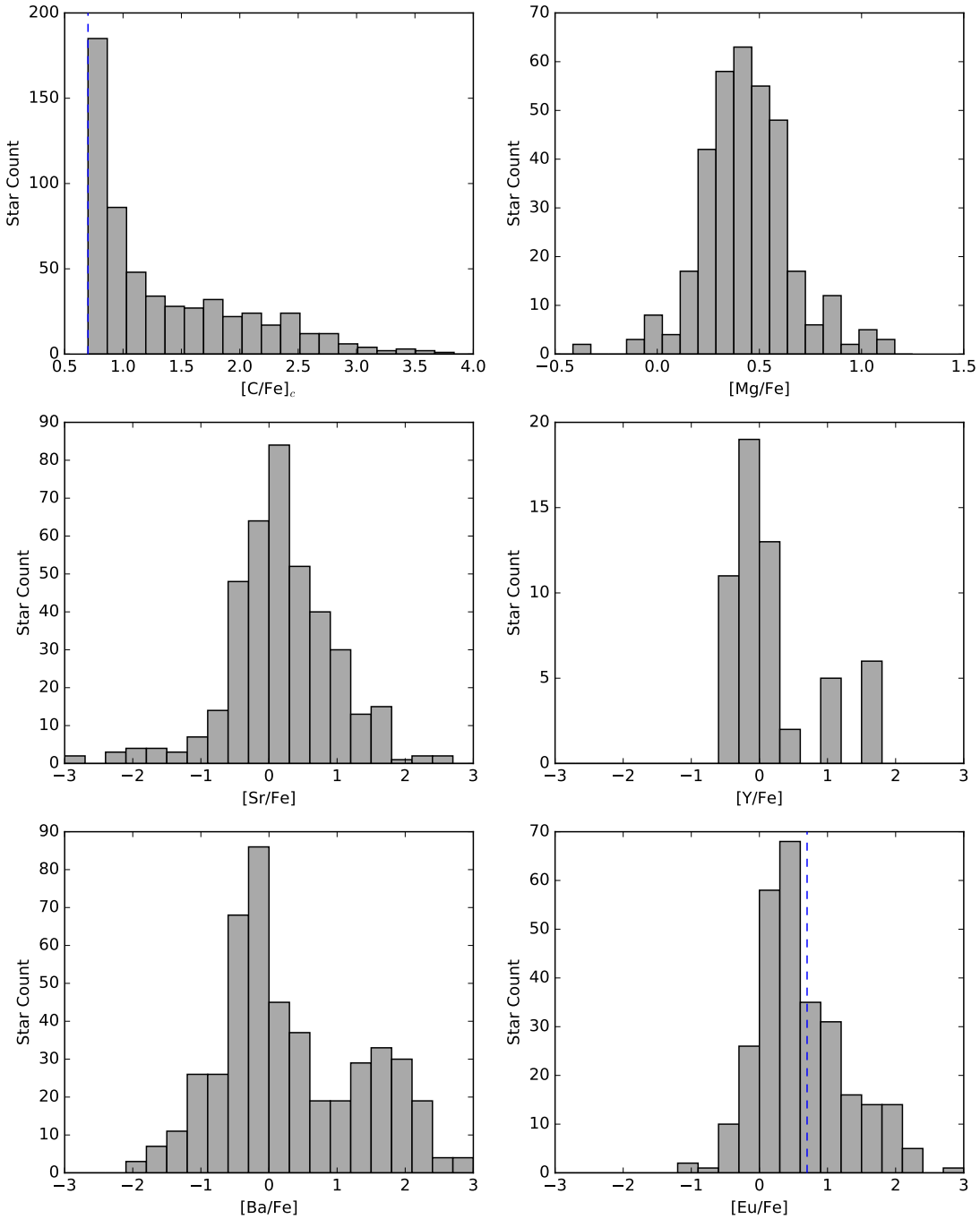


Figure 2. Histograms of the abundances for the Initial Sample of CEMP stars. From left to right, starting at the top, the histograms are as follows: [C/Fe]$_c$, [Mg/Fe], [Sr/Fe], [Y/Fe], [Ba/Fe], and [Eu/Fe]. The blue dashed blue line on the the [Eu/Fe] histogram indicates the r-II star boundary ([Eu/Fe] $> +0.7$).

tion. Section 3 provides a brief overview of the HDBSCAN clustering method we employ, and the results of its application to the CEMP sample. Section 4 examines the CDTGs based on the MW substructures and globular clusters that are associated with our CDTGs. In Section 5 we perform a statistical analysis of our results, and demonstrate the likely shared chemical-enrichment history of the members of the individual CDTGs. We also consider the nature of CDTGs based on clustering of the Group I and Group II CEMP stars in the Yoon-Beers Diagram. Section 6 considers the astrophysical implications of our results, and provides perspectives for future studies. Section 7 summarizes our final results.

2. DATA

A compilation of CEMP stars with abundance analyses based on high-resolution spectroscopy was published by Yoon et al. (2016), and it serves as the basis for this work. We also include CEMP surveys with similar analyses – Sakari et al. (2018), Hansen et al. (2018), Ezzeddine et al. (2020), Holmbeck et al. (2020), Rasmussen et al. (2020), Zepeda et al. (2022), Pristine (Lucchesi et al. 2022), and GALAH (Buder et al. 2021).

Note that we have chosen to exclusively adopt reported abundances based on the local thermodynamical equilibrium (LTE) assumption. Exploration of the effects of the non-LTE assumption, in particular on the abundance estimates for carbon, can and will be undertaken in the future. Popa et al. (2022, A&A, submitted) have outlined an approach for obtaining non-LTE corrections specifically for the CH molecular feature (*G*-band), upon which the great majority of present high-resolution analyses depend for estimates of carbon. This is expected to lead to a correction grid covering large ranges of stellar parameters, which will be of general utility. Note that Popa et al. specifically caution against the naive *combination* of non-LTE corrections with 3D effects, as some have attempted in the past; the 3D corrections are still in their relative infancy, and ideally need to be carried out in conjuction with non-LTE assumptions, not separately.

The use of large-scale photometric surveys, e.g., J-PLUS (Cenarro et al. 2019) and S-PLUS (Mendes de Oliveira et al. 2019) will be crucial for identification of many additional relatively bright CEMP stars for future high-resolution spectroscopic follow-up. Whitten et al. (2019) and Whitten et al. (2021) have already explored methodology for extracting estimates of [Fe/H] and [C/Fe] from the narrow- and broad-band photometry that they provide. Yang et al. (in preparation) is in the process of extending the elemental-abundance information in these surveys to encompass estimates not only for [Fe/H] and [C/Fe], but for [N/Fe], [Mg/Fe], and [Ca/Fe] as well.

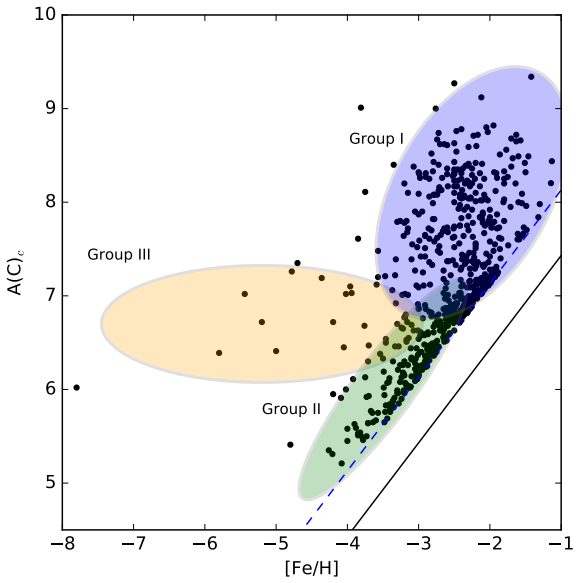


Figure 3. The Yoon-Beers Diagram of the Initial Sample of CEMP stars, showing the evolutionary corrected absolute carbon abundance, $A(\mathrm{C})_c$, as a function of [Fe/H]. The dotted blue line indicates $[\mathrm{C/Fe}]_c = +0.7$, which is the CEMP cutoff. For reference, the solid black line corresponds to $[\mathrm{C/Fe}]_c = 0$.

2.1. *Construction of the Initial Sample*

The data used in this work was assembled from the literature, including the sources cited in Yoon et al. (2016), JINABase (Abohalima & Frebel 2018), the SAGA database (Suda et al. 2008), and a number of other recent sources. We included stars with estimated stellar parameters, [Fe/H], and [C/Fe], at a minimum. When available, we also tabulated the [Mg/Fe] ratio and the neutron-capture elemental-abundance ratios [Sr/Fe], [Y/Fe], [Ba/Fe], and [Eu/Fe]. Duplicates were then removed, retaining the observations of a given star with the higher spectroscopic resolution and additional elemental abundances (in particular n-capture species) available. It is unavoidable that the methods used by the different sources are quite inhomogeneous; for this reason we choose not to combine the reported stellar parameter or abundance information when multiple sources exist for a given star.

We then removed stars that did not satisfy $[\mathrm{C/Fe}]_c > +0.7$, obtained by applying the carbon-abundance correction scheme for evolution on the giant branch (Placco et al. 2014). Following these cuts, our Initial Sample

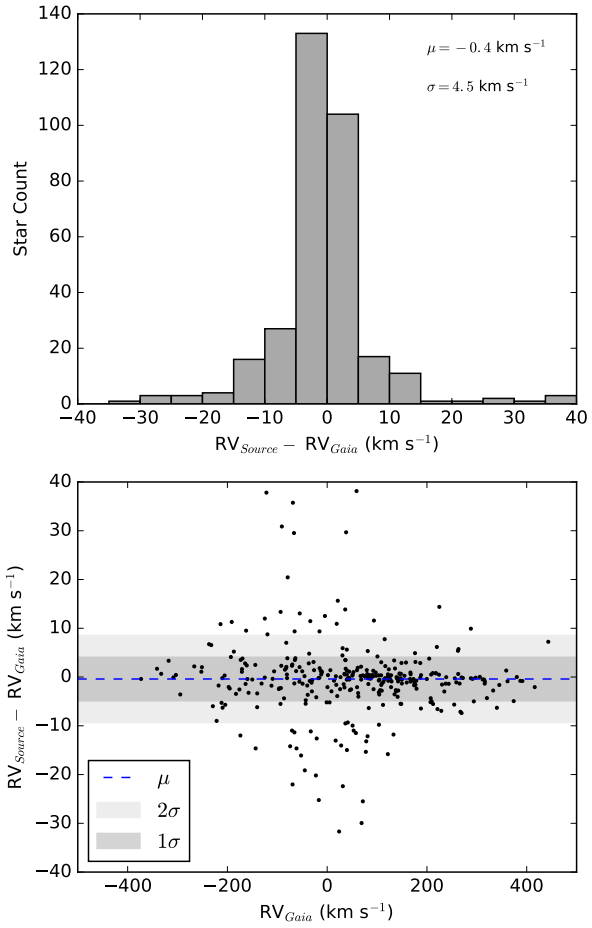


Figure 4. Top Panel: Histogram of the differences between the Source and *Gaia* values of radial velocity. Bottom Panel: The residuals between the Source and *Gaia* values of radial velocities, as a function of the *Gaia* radial velocity. The dotted blue line shows the mean of the residuals (−0.4 km s^{-1}). The dark and light shaded regions correspond to 1σ (4.5 km s^{-1}) and 2σ (9.0 km s^{-1}) error in the residuals, respectively.

consists of 644 stars. This sample includes stars with $3540 \leq T_{\rm eff}({\rm K}) \leq 7100$, surface gravity $-0.30 \leq \log g \leq 5.07$, $-7.80 \leq$ [Fe/H] ≤ -1.13, and $+0.71 \leq$ [C/Fe]$_c \leq +4.39$. The spatial distribution of the stars in our Initial Sample of CEMP stars are shown in Figure 1. Table 11 in the Appendix lists the various data for these stars. In the print edition, only the table description is provided; the full table is available only in electronic form.

Figure 2 provides histograms of the full set of elemental-abundance ratios considered in the present work.

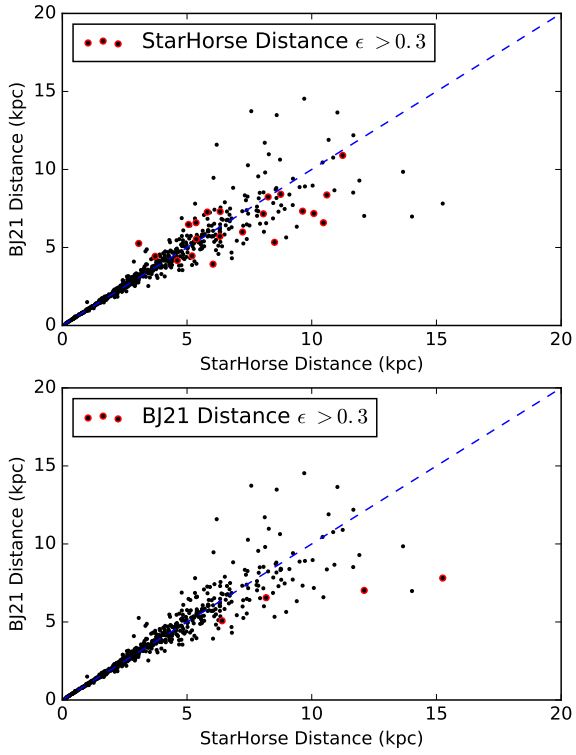


Figure 5. A comparison of the distance estimates from StarHorse (Anders et al. 2022) and Bailer-Jones (Bailer-Jones et al. 2021) for stars in the Initial Sample. Top Panel: Bailer-Jones distance as a function of StarHorse distance with stars with StarHorse relative distance errors $\epsilon > 30\%$ highlighted in red. Bottom Panel: Bailer-Jones distance as a function of StarHorse distance with stars with Bailer-Jones relative distance errors $\epsilon > 30\%$ highlighted in red. The blue-dashed line in both panels indicates a one-to-one comparison.

The Yoon-Beers Diagram of $A({\rm C})_{\rm c}$ vs. [Fe/H] for these stars is shown in Figure 3, corrected from the observed value to account for the depletion of carbon on the giant branch following Placco et al. (2014). The definitions of CEMP morphological groups were originally presented in Yoon et al. (2016), based on the level of [Ba/Fe]. These same authors demonstrated that similar assignments can be carried out using a separation based on $A({\rm C})_{\rm c}$ (and [Fe/H]) alone. As not all of our CEMP stars have available measured [Ba/Fe], we base our morphological group assignments purely on corrected carbon abundances, $A({\rm C})_{\rm c}$, [C/Fe]$_c$, and [Fe/H]. To account for the errors in these measurements, and the lack of clear delineations between the groups, we use definitions with some overlap. We assign CEMP groups as follows: Stars with [Fe/H] > -4 and $A({\rm C})_{\rm c} > 6.75$ are Group I stars,

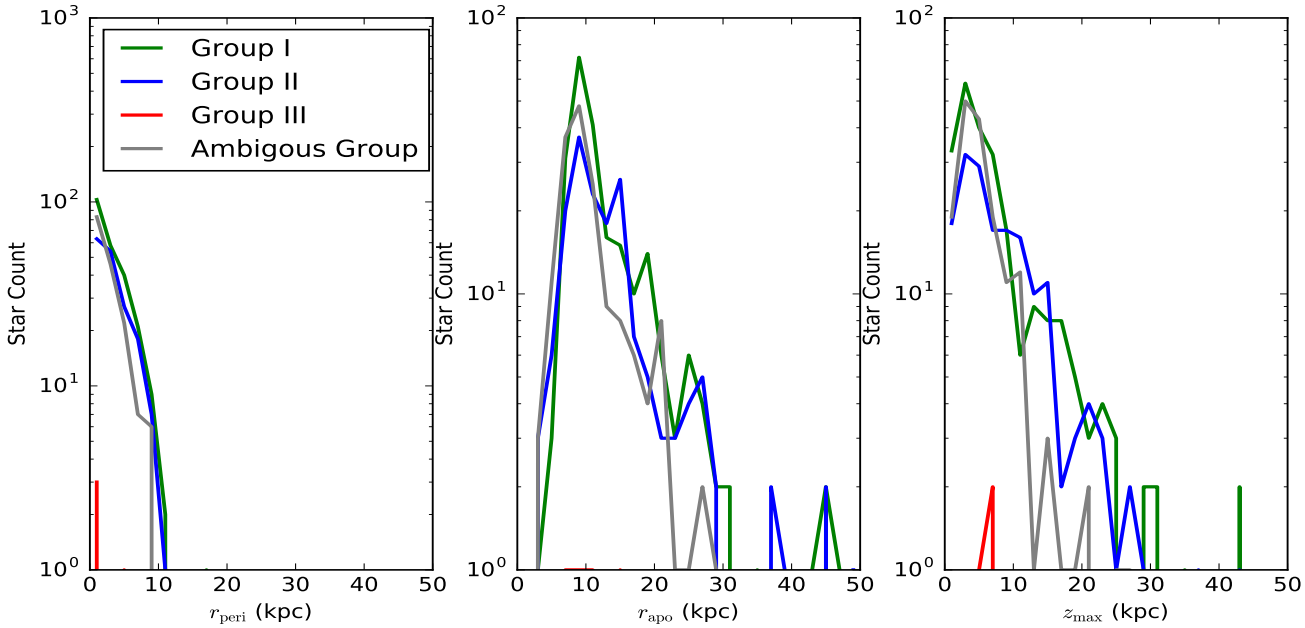


Figure 6. Distributions of $r_{\rm peri}$, $r_{\rm apo}$, and $Z_{\rm max}$, from left to right. The stars are separated into their Yoon-Beers CEMP morphological groups, as indicated in the left panel. Stars that were unbound from the Galaxy according to the `AGAMA` results are not included.

stars with $A(C)_c < 7.25$ and $[C/Fe]_c < +2.25$ are Group II stars, and all other stars are assigned to Group III. With these definitions, we have 443 Group I stars (271 Group I only stars), 363 Group II stars (191 Group II only stars), and 10 Group III stars. For convenience, a list of the stars with their adopted CEMP Group status and a summary of their available elemental-abundance ratios is provided in Table 2. Note that this table includes all stars in the Initial Sample of CEMP stars. Those that are removed in the assembly of the Final Sample, as described below, are listed with an asterisk following their names.

2.2. *Construction of the Final Sample*

2.2.1. *Radial Velocities, Distances, and Proper Motions*

To obtain the dynamical information for our Initial Sample we cross-matched our stars with *Gaia* EDR3 (Gaia Collaboration et al. 2016, 2021), supplemented by recent radial velocity information from *Gaia* DR3 (Babusiaux et al. 2022), in order to obtain radial velocities, parallaxes, and proper motions. When an accurate radial velocity was available from the spectroscopic surveys (which applies to all but a handful of cases), we use it if there was no *Gaia* RV. For stars with available Source radial velocities, Figure 4 compares these values with those having *Gaia* radial velocities. If the spectroscopic Source radial velocities differed from those reported by *Gaia* by more than 15 km s^{-1} (45 stars), the star was removed from further analysis, as many are suspected to be binaries.

Distance estimates for our stars were obtained using StarHorse (Anders et al. 2022). When the relative error from StarHorse exceeded 30%, we used the Bailer-Jones (Bailer-Jones et al. 2021) estimates, unless its relative error was also greater than 30%, in which case we removed the star from the sample. Figure 5 shows the distance estimates from both methods for stars in the Initial Sample. Note that three stars with unusually high, and likely suspect, distances were removed from the Final Sample.

2.2.2. *Dynamical Parameters*

We employ the Action-based GAlaxy Modelling Architecture[2] (`AGAMA`) package (Vasiliev 2018), which uses the radial velocities, distances, and proper motions of stars to derive orbital parameters for stars in the Initial sample. We use the same Solar position, Solar peculiar motions[3], and gravitational potential (McMillan 2017) as used in Shank et al. (2022b). To obtain errors for

[2] http://github.com/GalacticDynamics-Oxford/Agama

[3] We adopt a Solar position of (−8.249, 0.0, 0.0) kpc (Gravity Collaboration et al. 2020) and Solar peculiar motion in (U,W) as (11.1,7.25) km s^{-1} (Schönrich et al. 2010), with Galoctocentric Solar azimuthal velocity V = 250.70 km s^{-1} determined from Reid & Brunthaler (2020).

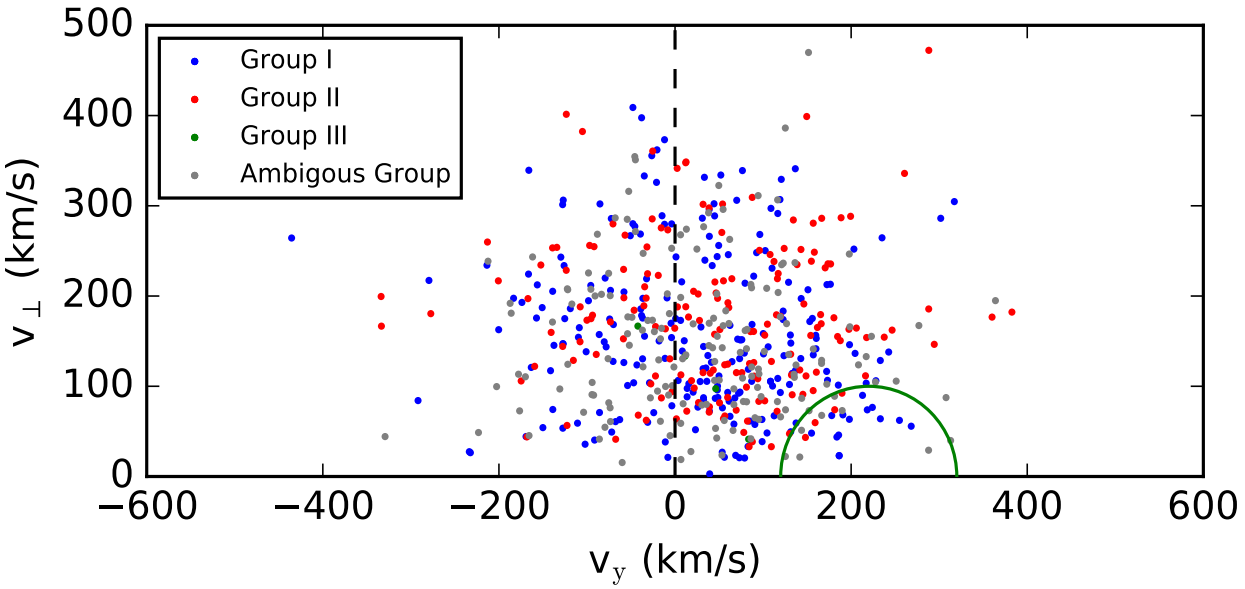


Figure 7. The Toomre Diagram of the Final Sample. The axes are $v_\perp = \sqrt{v_x^2 + v_z^2}$ vs. v_y. The green circle represents the location of 100 km s^{-1} from the Local Standard of Rest (232 km s^{-1}), while the vertical black dashed line represents the division between prograde ($v_y > 0$ km s^{-1}) and retrograde ($v_y < 0$ km s^{-1}) stellar orbits. The Group I stars are indicated as blue points, Group II stars are indicated as red points, Group III stars are indicated as green points, and the stars with ambiguous Group assignments are plotted in gray.

these estimates, we assume the errors in the input quantities are normally distributed. Then we obtain orbital parameters by finding the mean and standard deviation of the values from 1,000 runs of `AGAMA` sampling from the distributions for our inputs.

Figure 6 presents histograms of the derived estimates of $r_{\rm peri}$, $r_{\rm apo}$, and $Z_{\rm max}$; stars that were unbound from the Galaxy (E > 0 km^2 s^{-2}) are not included. All of the stars have $r_{\rm peri}$ distances inside of 20 kpc. As can be appreciated from inspection, the distributions of these parameters are quite similar across the Group I and Group II sub-samples. There are too few Group III stars to make meaningful interpretations at present.

The stars with `AGAMA` results consistent with being bound to the Galaxy comprise our Final Sample, which includes a total of 572 stars. Table 12 in the Appendix lists the various data for these stars. In the print edition, only the table description is provided; the full table is available only in electronic form.

Figure 7 is a Toomre Diagram of the stars in the Final Sample. For this sample, 64% of the stars are on prograde orbits, while 36% are on retrograde orbits. When we consider the stars that are assigned (unique) morphological groups, Group I stars are 62%/38% prograde/retrograde. Group II stars are 68%/32% prograde/retrograde. The Group III stars are 75%/25% prograde/retrograde. Note that not all stars in the Final Sample have morphological groups assigned, so these numbers are based on the subset that do.

Table 3. Identified CDTGs

CDTG	*N* Stars	Confidence	Associations
1	17	100.0%	H22:DTC-24, IR18:A, DG21:CDTG-11, H22:DTC-3, DS22b:DTG-51, DG21:CDTG-16 IR18:C, H22:DTC-4, DG21:CDTG-3
2	12	99.8%	GL21:DTG-31, H22:DTC-16, DS22a:DTG-50, GC21:Sequoia, KM22:Fimbulthul, DS22b:DTG-18
3	11	58.2%	I'itoi, GM18b:Rg5, GL21:DTG-6, KM22:C-3, KM22:Gaia-6
4	10	91.1%	GSE, AH17:VelHel-6, H22:DTC-3, KM22:C-3, DS22b:DTG-137

Table 3 *continued*

Table 3 *(continued)*

CDTG	*N* Stars	Confidence	Associations
5	10	78.5%	GSE, KM22:C-3
6	10	99.2%	Thamnos, DG21:CDTG-27, ZY20b:DTG-33, HL20:GR-2, H22:DTC-16, GC21:Sequoia, KM22:Gunnthra KM22:C-3, KM22:Gaia-6, EV21:NGC 6235, EV21:NGC 6356
7	9	83.5%	GSE, SL22:3, DS22b:DTG-27, DS22b:DTG-7
8	9	98.3%	GSE, GL21:DTG-34, H22:DTC-2, DS22b:DTG-95, DG21:CDTG-28, DS22b:DTG-30 GC21:Sausage, DG21:CDTG-9, DG21:CDTG-13, GL21:DTG-28, SL22:1
9	9	99.9%	LMS-1, GL21:DTG-17, DS22b:DTG-38, FS19:IH, HL19:GL-1, KM22:C-3
10	8	100.0%	DS22b:DTG-22
11	8	68.2%	GSE, H22:DTC-15, DS22b:DTG-79, GM17:Comoving, DS22a:DTG-29, DS22b:DTG-20, DS22b:DTG-135
12	7	78.5%	HL19:GL-1, KM22:C-3, KM22:NGC7089
13	7	100.0%	DS22b:DTG-35
14	7	82.8%	DS22a:DTG-6, GL21:DTG-4, H22:DTC-1, KM22:C-3
15	6	64.7%	LMS-1, H22:DTC-29, FS19:OH, KM22:C-3
16	6	80.6%	GSE, DG21:CDTG-21, H22:DTC-3, KM22:NGC7089
17	6	93.1%	GSE, SL22:59, H22:DTC-22, SM20:Sausage, GC21:Sausage
18	6	98.7%	DS22a:DTG-6
19	5	100.0%	new
20	5	54.8%	GSE, DS22b:DTG-12, EV21:Ryu 879 (RLGC 2)
21	5	99.7%	Thamnos, DS22b:DTG-170, DS22a:DTG-51, GL21:DTG-31, SM20:SeqG1, GC21:Sequoia
22	5	77.2%	Splashed Disk
23	5	68.9%	FS19:IH, KM22:C-3
24	5	100.0%	DS22b:DTG-161
25	4	59.1%	GSE, GL21:DTG-11, SM20:Sausage, DG21:CDTG-21, GL21:DTG-21, DS22b:DTG-98, SL22:3
26	4	69.4%	DS22b:DTG-4, ZY20b:DTG-44, GM17:Comoving, KM22:C-3, DS22a:DTG-4
27	4	94.9%	new
28	4	100.0%	GSE
29	4	60.9%	GSE, GL21:DTG-34, GL21:DTG-35, FS19:P, SL22:3, GC21:Sausage, DS22b:DTG-168
30	4	68.2%	GSE, FS19:OH, FS19:IH, GM17:Comoving, SM20:Sausage
31	4	40.3%	GSE, DS22a:DTG-8, DS22b:DTG-156, GC21:Sausage, KM22:NGC7089
32	4	62.5%	FS19:IH, KM22:NGC7089, EV21:FSR 1758
33	4	71.2%	GSE, GL21:DTG-20
34	3	35.5%	GSE, GM17:Comoving, SM20:Sausage, GC21:Sausage, GL21:DTG-11, KM22:Hrid, DS22a:DTG-27 DS22b:DTG-50, SL22:7
35	3	61.6%	GSE, GL21:DTG-38, ZY20b:DTG-40, GC21:Sausage, DS22b:DTG-71
36	3	51.7%	GSE, DS22b:DTG-27, DS22b:DTG-45, GC21:Sausage, DS22a:DTG-17
37	3	68.4%	H22:DTC-4
38	3	57.7%	MWTD, DS22b:DTG-43, DS22a:DTG-44
39	3	58.6%	GSE, KM22:NGC7089
40	3	50.5%	GL21:DTG-19, GC21:Sequoia, EV21:Pfleiderer 2

NOTE—We adopt the nomenclature for previously identified DTGs and CDTGs from Yuan et al. (2020).

3. CLUSTERING PROCEDURE

To perform our clustering exercise, we employ `HDBSCAN`[4] (Campello et al. 2013). This method groups data by density in the phase space considered (orbital energies and cylindrical actions), then places the clusters into a hierarchy based on how they change when the requisite density belonging to a cluster changes. We refer the interested reader to Campello et al. (2013), and Shank et al. (2022b) for a full description of `HDBSCAN`. In our use of this algorithm, we set the following parameters: `~min_cluster_size` = 3, `~min_samples` = 3, `~cluster_selection_method` = `'leaf'`, `~prediction_data` = `~True~`,Monte Carlo samples set at 1000, and minimum confidence set to 20%. The `~min_cluster_size~`determines how small the clusters can be. The `~min_samples~`parameter can be adjusted to account for different noise levels in the

[4] For a detailed description of the `HDBSCAN` algorithm visit: https://hdbscan.readthedocs.io/en/latest/how_hdbscan_works.html

Table 4. CDTGs Identified by HDBSCAN

NAME	[Fe/H]	$[C/Fe]_c$	[Mg/Fe]	[Sr/Fe]	[Y/Fe]	[Ba/Fe]	[Eu/Fe]
CDTG-1							
Structure: Unassigned Structure							
Group Assoc: CDTG-3: Gudin et al. (2021)							
Group Assoc: DTG-51: Shank et al. (2022a)							
Stellar Assoc: BPS CS 31078-0018 (DTC-24: Hattori et al. 2022)							
Stellar Assoc: HE 0430-4901 (A: Roederer et al. 2018)							
Stellar Assoc: HE 0430-4901 (CDTG-11: Gudin et al. 2021)							
Stellar Assoc: HE 0430-4901 (DTC-3: Hattori et al. 2022)							
Stellar Assoc: J100824.90-231412.0 (DTG-51: Shank et al. 2022a)							
Stellar Assoc: RAVE J192819.9-633935* (CDTG-16: Gudin et al. 2021)							
Stellar Assoc: CS 22945-017 (C: Roederer et al. 2018)							
Stellar Assoc: BPS CS 22945-0017 (CDTG-16: Gudin et al. 2021)							
Stellar Assoc: BPS CS 22945-0017 (DTC-4: Hattori et al. 2022)							
Globular Assoc: No Globular Associations							
Dwarf Galaxy Assoc: No Dwarf Galaxy Associations							
HE 0017−4346	−3.07	+3.02	+0.86	+0.84	...	+1.23	+0.99
RAVE J014908.0−491143	−2.94	+0.77	...	−0.45	...	−0.59	+0.09
BPS CS 31078−0018	−3.02	+0.74	...	...	...	+0.08	...
HE 0430−4901	−3.10	+1.00	...	...	...	...	...
RAVE J053817.0−751621	−2.03	+0.78	...	−0.63	...	−0.24	+0.44
LAMOST J070542.30+255226.6	−3.19	+1.78	+1.04	...	...	...	...
2MASS J09294972−2905589	−2.32	+0.75	+0.23	−0.36	...	−0.37	+0.14
RAVE J100824.9−231412	−1.95	+0.78	...	...	...	+0.36	−0.19
HE 1105+0027	−2.42	+1.96	+0.45	+0.83	...	+2.40	+1.80
2MASS J11580127−1522179	−2.41	+1.01	+0.20	−0.37	...	−1.07	+0.15
GALAH 150209004501153	−1.61	+0.79	...	...	+1.54	+0.36	...
Pristine J209.9364+15.9251	−2.25	+2.18	+0.22	+0.62	...	...	...
HE 1413−1954	−3.22	+1.44	...	−0.34	...	...	...
HD 187216	−2.50	+1.70	...	...	...	+2.00	+1.66
RAVE J192819.9−633935	−2.23	+0.76	+0.61	...	...	+0.09	+0.45
HE 2150−0825	−1.98	+1.31	+0.33	+0.75	...	+1.65	...
BPS CS 22945−0017	−2.73	+1.78	+0.26	+0.38	...	+0.48	+1.13
$\boldsymbol{\mu \pm \sigma([X/Y])}$	$\mathbf{-2.52 \pm 0.51}$	$\mathbf{+1.09 \pm 0.62}$	$\mathbf{+0.34 \pm 0.28}$	$\mathbf{+0.11 \pm 0.62}$	$\mathbf{+1.54 \pm ...}$	$\mathbf{+0.41 \pm 1.04}$	$\mathbf{+0.57 \pm 0.71}$

NOTE—$\boldsymbol{\mu}$ and $\boldsymbol{\sigma}$ represent the biweight estimates of the location and scale for the abundances in the CDTG.

NOTE—This table is a stub; the full table is available in the electronic edition.

data. By choosing ˜`cluster_selection_method` = `'leaf'`˜we allow HDBSCAN to make smaller clusters with tighter orbital parameter values. With the ˜`prediction_data` = ˜`True`˜the method has memory of the nominal clusters for each run in the Monte Carlo procedure. Full descriptions of these input choices of parameters can be found in Shank et al. (2022b).

Table 3 lists the 40 identified CDTGs, along with the number of members, assigned confidence values, and associations to previously identified DTGs and CDTGs, as described below. Note that, even though we set the minimum confidence for cluster identification to 20.0%, the smallest confidence in this table is 35.5%; most are much higher. The average confidence level for the 40 CDTGs is 77.1%.

Table 4 provides a listing of the individual members of the identified CDTGs from the application of HDBSCAN, along with the available elemental-abundance ratios considered in this paper. The biweight location and scale, analogous to the mean and standard deviation, for the abundances within each CDTG are shown in bold at the end of each listing. In addition, any stars that are associated with DTGs, CDTGs, globular clusters, or dwarf galaxies identified in previous works are listed at the beginning of each CDTG in the table.

Table 5. Cluster Dynamical Parameters Determined by `AGAMA`

Cluster	N Stars	$(\langle v_r\rangle,\langle v_\phi\rangle,\langle v_z\rangle)$	$(\langle J_r\rangle,\langle J_\phi\rangle,\langle J_z\rangle)$	$\langle E\rangle$	$\langle ecc\rangle$
		$(\sigma_{\langle v_r\rangle},\sigma_{\langle v_\phi\rangle},\sigma_{\langle v_z\rangle})$	$(\sigma_{\langle J_r\rangle},\sigma_{\langle J_\phi\rangle},\sigma_{\langle J_z\rangle})$	$\sigma_{\langle E\rangle}$	$\sigma_{\langle ecc\rangle}$
		(km s^{-1})	(kpc km s^{-1})	(10^5 km^2 s^{-2})	
CDTG−1	17	(56.3,154.2,−11.2)	(161.2,1273.1,63.0)	−1.642	0.38
		(74.3,18.2,50.3)	(61.8,69.6,40.1)	0.024	0.07
CDTG−2	12	(−18.5,−88.6,−19.1)	(291.4,−562.3,83.2)	−1.824	0.63
		(84.5,25.3,40.9)	(80.3,87.1,41.9)	0.040	0.07
CDTG−3	11	(−15.6,−134.2,−95.6)	(156.7,−911.0,707.2)	−1.534	0.37
		(104.5,48.2,170.6)	(79.4,178.2,128.5)	0.041	0.11
CDTG−4	10	(−60.3,69.3,−62.1)	(396.6,550.6,165.3)	−1.722	0.70
		(91.0,21.5,75.7)	(27.5,93.6,44.6)	0.021	0.03
CDTG−5	10	(−63.4,−13.5,67.3)	(314.9,−63.4,628.9)	−1.728	0.72
		(93.0,22.3,139.7)	(42.5,146.9,53.5)	0.024	0.06
CDTG−6	10	(1.4,−120.7,−13.2)	(137.0,−875.8,266.7)	−1.704	0.41
		(55.7,26.5,119.5)	(69.3,140.7,99.1)	0.049	0.10
CDTG−7	9	(2.2,33.6,26.5)	(499.3,259.5,74.2)	−1.814	0.84
		(61.2,15.2,78.2)	(71.1,119.0,29.5)	0.018	0.08
CDTG−8	9	(148.2,−22.6,−13.2)	(811.8,−186.6,20.3)	−1.678	0.92
		(35.4,10.4,37.3)	(51.7,88.7,63.9)	0.036	0.04
CDTG−9	9	(60.4,100.0,−68.5)	(180.3,699.4,584.0)	−1.620	0.44
		(56.5,33.0,174.3)	(45.3,55.8,90.2)	0.038	0.06
CDTG−10	8	(53.3,111.9,3.6)	(242.0,879.4,144.2)	−1.707	0.52
		(55.4,7.3,64.6)	(8.3,47.9,29.2)	0.022	0.01
CDTG−11	8	(8.4,27.1,10.8)	(400.9,146.8,183.3)	−1.861	0.88
		(133.7,18.4,89.6)	(58.7,84.3,33.8)	0.050	0.06
CDTG−12	7	(−37.2,83.2,−16.2)	(268.9,604.6,302.0)	−1.715	0.58
		(90.8,8.7,81.3)	(40.1,60.3,52.2)	0.018	0.03
CDTG−13	7	(−15.9,188.7,−2.2)	(31.8,1552.4,37.3)	−1.634	0.17
		(18.5,2.5,37.0)	(7.5,61.9,28.3)	0.024	0.03
CDTG−14	7	(−2.8,15.9,−218.0)	(246.5,−7.9,1410.4)	−1.454	0.44
		(123.0,89.4,76.2)	(87.1,440.2,105.3)	0.055	0.06
CDTG−15	6	(−67.5,73.2,−95.7)	(455.8,413.2,972.8)	−1.487	0.60
		(123.5,54.2,131.9)	(113.3,176.5,49.1)	0.051	0.10
CDTG−16	6	(−31.1,51.3,23.1)	(810.1,457.0,188.6)	−1.530	0.83
		(174.9,15.7,78.6)	(16.7,63.8,59.7)	0.035	0.03
CDTG−17	6	(−155.2,−21.4,58.9)	(1284.8,−158.1,515.3)	−1.368	0.95
		(153.1,8.7,144.5)	(72.6,80.5,97.6)	0.028	0.03
CDTG−18	6	(87.8,−12.0,165.9)	(148.8,−90.4,1917.9)	−1.407	0.30
		(113.5,20.8,214.4)	(163.8,187.0,113.4)	0.049	0.14
CDTG−19	5	(17.5,178.6,41.8)	(42.1,1122.0,197.8)	−1.703	0.20
		(45.7,34.7,112.3)	(33.6,21.2,4.2)	0.020	0.09
CDTG−20	5	(51.6,29.9,3.2)	(618.5,279.8,194.6)	−1.682	0.86
		(56.3,12.5,78.7)	(21.6,138.9,16.6)	0.033	0.06
CDTG−21	5	(−18.4,−128.9,28.0)	(254.5,−901.7,80.4)	−1.688	0.54
		(96.6,15.6,66.9)	(28.0,79.0,43.4)	0.033	0.00
CDTG−22	5	(−41.8,74.5,95.7)	(76.0,287.0,491.7)	−1.873	0.44
		(21.6,29.1,29.9)	(33.2,45.6,70.7)	0.058	0.07
CDTG−23	5	(38.0,85.6,60.9)	(77.4,420.3,672.2)	−1.739	0.34
		(98.2,3.3,144.4)	(68.7,45.7,61.4)	0.017	0.20
CDTG−24	5	(17.8,232.0,0.9)	(59.1,1995.8,57.5)	−1.503	0.20
		(63.5,19.8,54.5)	(7.3,144.6,44.5)	0.015	0.02
CDTG−25	4	(−12.9,−8.6,40.5)	(1279.9,−127.7,98.7)	−1.454	0.92
		(181.4,17.7,44.1)	(80.3,214.4,21.3)	0.041	0.02

Table 5 *continued*

Table 5 *(continued)*

Cluster	N Stars	$(\langle v_r\rangle,\langle v_\phi\rangle,\langle v_z\rangle)$	$(\langle J_r\rangle,\langle J_\phi\rangle,\langle J_z\rangle)$	$\langle E\rangle$	$\langle ecc\rangle$
		$(\sigma_{\langle v_r\rangle},\sigma_{\langle v_\phi\rangle},\sigma_{\langle v_z\rangle})$	$(\sigma_{\langle J_r\rangle},\sigma_{\langle J_\phi\rangle},\sigma_{\langle J_z\rangle})$	$\sigma_{\langle E\rangle}$	$\sigma_{\langle ecc\rangle}$
		(km s^{-1})	(kpc km s^{-1})	(10^5 km^2 s^{-2})	
CDTG−26	4	(9.9,−22.5,4.1)	(113.7,−164.1,983.4)	−1.672	0.38
		(117.7,28.2,176.3)	(50.9,207.4,27.6)	0.039	0.08
CDTG−27	4	(43.5,282.5,−3.3)	(224.6,2492.1,54.7)	−1.340	0.34
		(49.8,38.6,38.8)	(54.5,100.3,33.6)	0.034	0.04
CDTG−28	4	(−124.6,−22.5,−23.8)	(145.5,−57.3,113.6)	−2.174	0.84
		(24.1,31.3,81.8)	(61.2,98.6,4.1)	0.026	0.02
CDTG−29	4	(−118.0,12.5,−46.0)	(711.6,95.5,55.7)	−1.739	0.93
		(34.3,13.2,27.8)	(19.6,110.1,14.3)	0.011	0.05
CDTG−30	4	(−10.9,−11.4,58.0)	(1167.6,−104.5,801.2)	−1.338	0.89
		(233.9,12.6,160.9)	(87.7,128.6,35.8)	0.023	0.03
CDTG−31	4	(160.9,21.2,−13.7)	(978.3,164.9,314.1)	−1.503	0.94
		(47.6,2.9,122.9)	(59.5,53.2,43.3)	0.048	0.02
CDTG−32	4	(62.7,124.8,−34.3)	(519.3,1062.6,255.6)	−1.509	0.61
		(142.4,43.6,94.7)	(104.0,82.1,21.4)	0.031	0.05
CDTG−33	4	(35.7,−67.7,21.4)	(889.2,−573.3,91.3)	−1.503	0.83
		(219.1,17.6,67.2)	(20.8,148.6,31.4)	0.035	0.04
CDTG−34	3	(129.6,26.3,−70.7)	(1593.8,181.2,63.7)	−1.345	0.93
		(277.3,44.7,19.3)	(67.9,393.4,16.2)	0.036	0.04
CDTG−35	3	(69.8,−2.8,−17.6)	(663.7,−22.2,37.7)	−1.814	0.98
		(39.7,3.9,25.7)	(22.1,31.4,13.4)	0.014	0.01
CDTG−36	3	(19.5,12.3,8.0)	(516.0,81.5,103.8)	−1.851	0.95
		(97.3,8.8,53.2)	(34.3,59.3,23.3)	0.021	0.03
CDTG−37	3	(5.9,189.1,32.9)	(38.6,891.0,181.2)	−1.796	0.23
		(51.9,17.9,78.0)	(21.9,59.6,22.5)	0.023	0.07
CDTG−38	3	(32.0,111.4,41.5)	(174.9,701.8,63.1)	−1.861	0.49
		(27.3,8.8,26.3)	(18.5,61.3,5.5)	0.024	0.04
CDTG−39	3	(−222.0,88.6,−25.1)	(860.9,548.3,377.3)	−1.456	0.80
		(64.6,30.7,95.3)	(38.1,36.5,42.0)	0.016	0.01
CDTG−40	3	(61.2,−116.4,55.7)	(389.1,−1050.4,96.5)	−1.599	0.58
		(105.2,19.8,23.5)	(20.4,95.9,50.0)	0.014	0.03

Table 5 lists the mean values, along with the associated dispersions, of the dynamical parameters for the CDTGs. The number of stars in each CDTG is indicated by the N Stars column.

4. STRUCTURE ASSOCIATIONS

4.1. *Milky Way Substructures*

We check each CDTG for association with known MW substructures. These associations are based on the stellar orbital parameters as well as the chemical abundances of individual stars in the CDTGs. To find these associations we employ the substructure criteria from Naidu et al. (2020). Each substructure has specific dynamical and chemical criteria, and CDTGs are associated to these substructures when the criteria are met. To see exactly how these criteria are applied, we refer the interested reader to Shank et al. (2022a). We found that 25 of the 40 CTDGs had associated substructures: Gaia-Sausage-Enceladus (GSE), LMS-1 (Wukong), the Metal-Weak Thick Disk (MWTD), Thamnos, I'itoi, and the Splashed Disk listed in Table 6. This table provides the numbers of stars in the CDTGs associated with each substructure, the means and dispersions of their chemical abundances, and the means and dispersions of their dynamical parameters. The Lindblad Diagram and projected-action plot for these substructures is shown in Figure 8. The CDTGs found to be associated with known MW substructures and globular clusters are listed in Table 7.

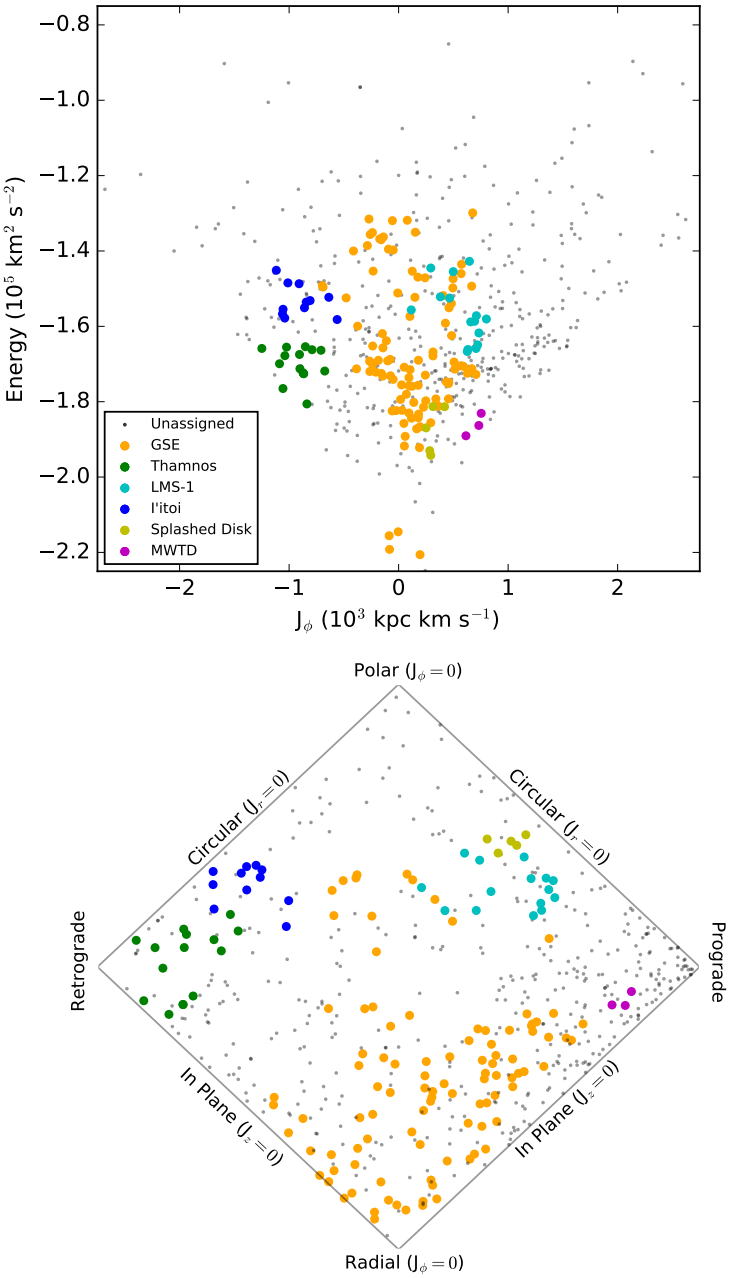


Figure 8. Locations of the CEMP CDTG stars in two orbital-parameter phase spaces. Top Panel: Lindblad Diagram of the identified MW substructures. The different structures are associated with the colors outlined in the legend. The gray points are the stars from the Final Sample that are not assigned to any CDTGs. Bottom Panel: The projected-action plot of the same substructures. This space is represented by J_ϕ/J_{Tot} for the horizontal axis and $(J_z - J_r)/J_{Tot}$ for the vertical axis with $J_{Tot} = J_r + |J_\phi| + J_z$. For more details on the projected-action space, see Figure 3.25 in Binney & Tremaine (2008).

4.1.1. *Gaia-Sausage-Enceladus*

One of the earliest known mergers, Gaia-Sausage-Enceladus (GSE), is thought to have been accreted by the MW about 10 Gyr ago (Helmi 2020). It is also the largest known merger, and the most populated substructure in this work, with 99 CEMP stars in 18 different CDTGs. While the metallicity distribution function for GSE peaks near [Fe/H] ~ -1.2, the CEMP stars associated with GSE exhibit a biweight location and scale (robust alternatives to the mean and standard deviation) of $\langle$[Fe/H]$\rangle = -2.52$ ($\sigma = 0.55$ dex). Our GSE stars also show a biweight location and scale of $\langle$[Mg/Fe]$\rangle = +0.40$ ($\sigma = 0.22$ dex), which is higher than GSE's value (+0.21; Naidu et al. 2022). Based on these differences, it is likely that the low-metallicity tail of GSE is comprised of CEMP stars with elevated [Mg/Fe] abundances.

4.1.2. *LMS-1 (Wukong)*

We found 2 CDTGs in the substructure LMS-1, with a total of 15 stars. LMS-1 was found to be the most metal-poor substructure by Malhan et al. (2022), so finding this large number of CEMP stars might be expected, given the increasing frequency of CEMP stars with declining metallicity. The CEMP stars associated with LMS-1 belong to all three CEMP Group morphologies. We found 3 UMP ([Fe/H] < -4) stars associated with LMS-1. No other substructure has more than 2 stars at or below [Fe/H] < -4, and there was only one such star in a CDTG without an associated substructure. Based on this, UMP stars are likely much more common in LMS-1 than in other recognized MW substructures, despite the mean of -1.58 reported by Naidu et al. (2022) for the substructure as a whole. For our sample, we found $\langle$[Fe/H]$\rangle = -3.11$ with a large dispersion of $\sigma = 0.78$ dex.

4.1.3. *Thamnos*

Thamnos is believed to have formed from the merging of a relatively small satellite (stellar mass $< 5 \times 10^6\ M_\odot$) with the MW (Helmi 2020). It is particularly interesting how low in energy the stars in this structure are, considering how deep in the MW it resides. This has been used to argue that the merger occurred very early in the MW's history (Bonaca et al. 2020; Kruijssen et al. 2020). We found 2 CDTGs associated with Thamnos, with 15 total CEMP stars, including both Group I and Group II CEMP morphologies. The stars in Thamnos have the second highest mean metallicity ($\langle$[Fe/H]$\rangle = -2.35$) among those with substructure associations, with a dispersion $\sigma = 0.30$ dex.

4.1.4. *The Metal-Weak Thick Disk*

The MWTD has been argued to have formed from either a merger scenario, possibly related to GSE, or the result of old stars born within the Solar radius migrating out to the Solar position due to tidal instabilities within the MW (Carollo et al. 2019). However, several recent papers, including Carollo et al. (2019), An & Beers (2020), Dietz et al. (2021), and Mardini et al. (2022), have presented evidence that the MWTD is an independent structure from the canonical thick disk, and thus may have arisen independently.

We found 1 CDTG of CEMP stars associated with this substructure, with a combined total of 3 stars. As expected, these stars occupy the low-metallicity tail of the MWTD Metallicity Distribution Function (MDF), with a biweight location and scale of $\langle$[Fe/H]$\rangle = -2.28$ ($\sigma = 0.20$ dex). The CEMP stars associated with the MWTD have a [Mg/Fe] biweight location and scale ($\langle$[Mg/Fe]$\rangle = +0.36$, $\sigma = 0.01$ dex) that is quite similar to the stars in GSE.

4.1.5. *I'itoi*

The substructure I'itoi has several possible formation scenarios suggested in the literature, associating it with other halo substructures, including Sequoia and Thamnos (Naidu et al. 2020). We found 1 CDTG in I'itoi that contains a total of 11 stars, including both Group I and Group II morphologies. We found I'itoi to be the second most metal-poor substructure among our associations, $\langle$[Fe/H]$\rangle = -2.71$) with a dispersion of $\sigma = 0.33$ dex.

4.2. *Splashed Disk*

The Splashed Disk (SD) is the second least-populated substructure found to be associated with our CEMP CDTGs. It is believed to have been formed when a component of the primordial disk was heated by the GSE merger, giving it its now characteristic kinematics (Naidu et al. 2020). The one CDTG associated with this substructure is unique for the fact the $[C/Fe]_c$ and [Mg/Fe] ratios have larger dispersions than any other substructures. and the [Fe/H] dispersions is the second largest of all the substructures. We note this as interesting, but don't have an explanation for why this might be besides the small statistics due to the limited number of stars.

4.3. *Previously Identified Dynamically Tagged Groups and Stellar Associations*

To further validate the results of these cluster associations with MW substructures, we employ the mean

Table 6. Identified Milky Way Substructures

Substructure	N Stars	$\langle$[Fe/H]$\rangle$	$\langle$[C/Fe]$_c\rangle$	$\langle$[Mg/Fe]$\rangle$	$\langle$[Sr/Fe]$\rangle$	$\langle$[Y/Fe]$\rangle$	$\langle$[Ba/Fe]$\rangle$	$\langle$[Eu/Fe]$\rangle$	$(\langle v_r\rangle,\langle v_\phi\rangle,\langle v_z\rangle)$	$(\langle J_r\rangle,\langle J_\phi\rangle,\langle J_z\rangle)$	$\langle E\rangle$	$\langle ecc\rangle$
									$(\sigma_{\langle v_r\rangle},\sigma_{\langle v_\phi\rangle},\sigma_{\langle v_z\rangle})$	$(\sigma_{\langle J_r\rangle},\sigma_{\langle J_\phi\rangle},\sigma_{\langle J_z\rangle})$	$\sigma_{\langle E\rangle}$	$\sigma_{\langle ecc\rangle}$
									(km s^{-1})	(kpc km s^{-1})	(10^5 km^2 s^{-2})	
GSE	99	−2.52	+1.31	+0.40	+0.29	+0.07	+0.38	+0.64	(−11.6,17.9,2.6)	(701.8,104.8,233.4)	−1.666	0.85
		0.55	0.73	0.22	0.74	0.22	1.00	0.62	(152.1,48.1,89.3)	(351.2,305.5,217.2)	0.195	0.10
Thamnos	15	−2.35	+1.27	+0.30	−0.10	*NaN*	+0.62	+0.68	(−15.0,−124.0,−0.2)	(177.9,−915.3,201.7)	−1.702	0.43
		0.30	0.53	0.28	1.33	*NaN*	1.11	0.54	(69.3,23.0,102.0)	(75.9,146.9,117.9)	0.043	0.10
LMS-1	15	−3.11	+1.44	+0.54	−0.27	*NaN*	−0.05	+0.41	(9.1,99.1,−50.5)	(293.2,579.4,742.5)	−1.567	0.52
		0.78	0.63	0.30	1.05	*NaN*	1.35	0.57	(106.7,47.7,137.7)	(152.1,185.2,201.7)	0.077	0.11
I'itoi	11	−2.71	+1.57	+0.41	+0.18	+0.20	+0.53	+0.58	(−21.7,−136.7,−37.7)	(184.5,−901.1,711.1)	−1.531	0.38
		0.33	0.74	0.06	0.35	0.00	1.35	1.00	(93.8,45.0,148.4)	(98.2,172.7,116.5)	0.040	0.11
Splashed Disk	5	−2.69	+1.23	+1.17	−0.18	+0.09	−0.03	+0.88	(−22.8,81.7,62.3)	(85.0,312.2,463.9)	−1.873	0.45
		0.63	0.90	0.59	0.26	0.34	0.98	0.39	(39.0,23.7,116.6)	(27.3,57.5,54.5)	0.055	0.07
MWTD	3	−2.28	+1.35	+0.36	+0.33	*NaN*	+0.33	+0.51	(32.0,111.4,41.5)	(174.9,701.8,63.1)	−1.861	0.49
		0.20	0.79	0.01	0.27	*NaN*	0.68	0.27	(27.3,8.8,26.3)	(18.5,61.3,5.5)	0.024	0.04

Table 7. Associations of Identified CDTGs

Structure	Reference	Associations	Identified CDTGs
MW Substructure	Naidu et al. (2020)	GSE	4, 5, 7, 8, 11, 16, 17, 20, 25, 28, 29, 30, 31, 33, 34, 35, 36, 39
		LMS-1	9, 15
		Thamnos	6, 21
		I'itoi	3
		MWTD	38
		Splashed Disk	22

group orbital properties of each CDTG to compare with previously identified CDTGs. We then make associations between stars in our CDTGs with previously DTGs, based on angular separation on the sky. We consider stars as being associated when the angular separation is within 5″.

The full list of CDTGs associated with DTGs, groups, streams, or populations from other works is shown in Table 8. For example, for CDTG-1 we found no substructure associations, but found it to be associated with DG21:CDTG-3 and DS22b:DTG-51 through the group mean orbital parameters, and found star-to-star associations with both of the aforementioned DTGs from Gudin et al. (2021); Shank et al. (2022a). While both CDTG-1 and DS22b:DTG-51 did not have associations with a MW substructure, DG21:CDTG-3 was associated with the MWTD. Based on the fact that CDTG-1 has 17 member stars, DS22b:DTG-51 has 11 member stars, and DG21:CDTG-3 only has 3 member stars, the stars in CDTG-1 are not likely connected to the MWTD, as DG21:CDTG-21 suggested.

If we examine the one of the most metal-poor CDTGs identified, CDTG-15, associated with LMS-1, we find that one member, HE 1310-0536, was inferred as being part of the MW outer halo by Sestito et al. (2019). This demonstrates the ability to find outer-halo substructures that are currently near their $r_{\rm peri}$, and thus more easily observable.

Another use for associating our CDTGs with previous studies is the ability to examine substructures with few associated CDTGs. We found only CDTG-3 associated with the I'itoi substructure. However, there are 2 CEMP stars with moderate r-process enhancement. Naidu et al. (2020) has argued that I'itoi, and the larger substructure it is a part of, forms the dominant component of the highly retrograde halo. This suggests that mergers associated with the highly retrograde halo may have preferentially experienced star-formation environments undergoing r-process enrichment. Clearly, this association of stars with a characteristic CEMP-r abundance signature is worthy of further study.

4.4. *Globular Clusters and Dwarf Galaxies*

In previous work using this methodology to find associations between CDTGs, DTGs, and MW substructures, globular clusters have frequently been identified as possibly linked to the dynamical clusters. However, of the 40 CDTGs found in this work, only 4 exhibit associations with globular clusters: CDTG-6, CDTG-20, CDTG-32, and CDTG-40. The first and second of these

CDTGs were found to be associated with Thamnos and GSE, respectively (the last two had no associated substructure). It is certainly of interest how few globular clusters can be associated with CEMP CDTGs, and worthy of investigation. CEMP stars have been shown by a number of authors to be rare in globular clusters (e.g., Kirby et al. 2015; Arentsen et al. 2021, and references therein). It has been suggested that the lack of CEMP-*s* (Group I) stars in globular clusters is due to the low rate of long-lived binary stars in these dense environments. The present work clearly supports this hypothesis. If CEMP-no (Group II) stars formed early, from gas enriched by the ejecta of high-mass supernovae (SNe), as we argue in this paper, their rarity in presently observed globular clusters might be expected.

5. CHEMICAL STRUCTURE OF THE IDENTIFIED CDTGS

5.1. *Statistical Framework*

Following Gudin et al. (2021), we perform a statistical analysis of our CDTGs to determine how probable the observed abundance dispersions for a given set of elements would be if their member stars were selected at random from the full set of CEMP stars in the Final Sample. To perform this analysis, we create 2.5×10^6 random groups of $3 \leq N \leq 12$ stars with dispersions based on the biweight scale (Beers et al. 1990). We then use this to generate cumulative distribution functions (CDFs) for the abundance distributions for each possible size of the random groups. This serves as a proxy for abundances we should expect in a CDTG of a given size. If, for a given element, the CDTGs preferentially populate the low end of the simulated CDFs, we infer that its members exhibit strong similarities in their abundances. We then use binomial and multinominal probabilities to calculate the statistical likelihoods of the distributions of the CDTG abundance dispersions based on the derived CDFs.

We calculate the statistical significance at three thresholds of CDF values ($\alpha \in \{0.25, 0.33, 0.5\}$) for each of the individual elemental abundances ($X \in \{[\mathrm{Fe/H}], [\mathrm{C/Fe}]_c, \dots\}$) of the CDTGs, as well the significance across all α values, or across all X abundances. These probabilities are defined as:

- *Individual Elemental-Abundance Dispersion (IEAD) probability*: Individual binomial probability for specific values of α and X.
- *Full Elemental-Abundance Distribution (FEAD) probability*: Multinomial probability for specific values of α, grouped over all abundances X.
- *Global Element Abundance Dispersion (GEAD) probability*: Multinomial probability for specific abundances X, grouped over all values of α. This is the overall statistical significance for the particular abundance.
- *Overall Element Abundance Dispersion (OEAD) probability*: Multinomial probability grouped over all values of α and all abundances X. This is the overall statistical significance of our clustering results.

For a more detailed discussion of the above probabilities, and their use, the interested reader is referred to Gudin et al. (2021).

5.2. *Important Caveats*

It should be noted this statistical analysis method requires that the elemental abundances of the parent sample of stars, the population that the clustering was performed on, has dispersions that are large enough that the individual CDTG elemental dispersions are sufficiently low in comparison. If the dispersions of the parent population are too small compared to the CDTGs for that element, the analysis will not be able to find distinctions between a random grouping of stars drawn from the parent population and the stars within a given CDTG. To aid in determining which elements this applies, we compare the Inter-Quartile Range (IQR) of the means of random draws from from the parent sample to the IQR of the means of the CDTGs for a given element. We adopt the rule of thumb that the mean IQR for each element of a CDTG is on the order of one-half of the IQR of the randomly drawn stars from the parent population. Otherwise, there is insufficient "dynamical range" for the statistical inferences to be made with confidence, at least for individual elements.

Table 8. Associations of Identified CDTGs with Previous Groups

Reference	Associations	Identified CDTGs
Shank et al. (2022a)	DTG-27	7, 36
	DTG-4	26
	DTG-7	7
	DTG-12	20
	DTG-135	11
	DTG-137	4
	DTG-156	31
	DTG-161	24
	DTG-168	29
	DTG-170	21
	DTG-18	2
	DTG-20	11
	DTG-22	10
	DTG-30	8
	DTG-35	13
	DTG-38	9
	DTG-43	38
	DTG-45	36
	DTG-50	34
	DTG-51	1
	DTG-71	35
	DTG-79	11
	DTG-95	8
	DTG-98	25
Limberg et al. (2021)	DTG-11	25, 34
	DTG-31	2, 21
	DTG-34	8, 29
	DTG-4	14
	DTG-6	3
	DTG-17	9
	DTG-19	40
	DTG-20	33
	DTG-21	25
	DTG-28	8
	DTG-35	29
	DTG-38	35
Hattori et al. (2022)	DTC-3	1, 4, 16
	DTC-4	1, 37
	DTC-16	2, 6
	DTC-1	14
	DTC-2	8
	DTC-15	11
	DTC-22	17
	DTC-24	1
	DTC-29	15
Shank et al. (2022b)	DTG-6	14, 18
	DTG-4	26
	DTG-8	31
	DTG-17	36
	DTG-27	34
	DTG-29	11
	DTG-44	38
	DTG-50	2
	DTG-51	21
Gudin et al. (2021)	CDTG-21	16, 25
	CDTG-3	1
	CDTG-9	8
	CDTG-11	1
	CDTG-13	8
	CDTG-16	1
	CDTG-27	6
	CDTG-28	8
Malhan et al. (2022)	C-3	3, 4, 5, 6, 9, 12, 14, 15, 23, 26
	NGC7089	12, 16, 31, 32, 39
	Gaia-6	3, 6
	Fimbulthul	2
	Gunnthra	6

Table 8 *continued*

Table 8 *(continued)*

Reference	Associations	Identified CDTGs
Malhan et al. (2022)	Hrid	34
Vasiliev & Baumgardt (2021)	FSR 1758	32
	NGC 6235	6
	NGC 6356	6
	Pfleiderer 2	40
	Ryu 879 (RLGC 2)	20
Lövdal et al. (2022)	3	7, 25, 29
	1	8
	59	17
	7	34
Sestito et al. (2019)	IH	9, 23, 30, 32
	OH	15, 30
	P	29
Yuan et al. (2020)	DTG-33	6
	DTG-40	35
	DTG-44	26
Cordoni et al. (2021)	Sausage	8, 17, 29, 31, 34, 35, 36
	Sequoia	2, 6, 21, 40
Monty et al. (2020)	Sausage	17, 25, 30, 34
	SeqG1	21
Roederer et al. (2018)	A	1
	C	1
Helmi et al. (2017)	VelHel-6	4
Li et al. (2019)	GL-1	9, 12
Li et al. (2020)	GR-2	6
Myeong et al. (2017)	Comoving	11, 26, 30, 34
Myeong et al. (2018)	Rg5	3

NOTE—We draw attention to the associations with CDTGs from Gudin et al. (2021) and Roederer et al. (2018) due to their enhancement in r-process abundances.

The statistical power of our comparisons increase with the numbers of CDTGs in a given parent population. This is ultimately the reason that we set the minimum number of stars per CDTG to 3, so that when we examine the sample divided into CEMP Group I and Group II morphologies, as described below, we retain a sufficiently large number of CDTGs (in particular for the Group II CEMPs) for meaningful statistical comparisons.

It should also be kept in mind that the observed CDTG elemental-abundance dispersions depend on a number of different parameters, including not only the total mass of a given parent dwarf galaxy, but on its available gas mass for conversion into stars, the history of star formation in that environment, and the nature of the progenitor population(s) involved in the production of a given element. These are complex and interacting sets of conditions, and certainly are best considered in the context of simulations (such as Hirai et al. 2022). Consequently, the expected result for a given element in a given set of CDTGs is not always clear. However, we have designed our statistical tests to consider a broad set of questions of interest, the most pertinent of which for the current application are the FEAD and OEAD probabilities, which we employ for making our primary inferences.

Table 9. CDTG Abundance Means, Dispersions and Inter-Quartile Ranges (IQR)

Cluster	N Stars	[Fe/H]	$[C/Fe]_c$	[Mg/Fe]	[Sr/Fe]	[Y/Fe]	[Ba/Fe]	[Eu/Fe]
CDTG-1	17	-2.52 ± 0.51	$+1.09 \pm 0.62$	$+0.34 \pm 0.28$	$+0.11 \pm 0.62$	$+1.54 \pm \ldots$	$+0.41 \pm 1.04$	$+0.57 \pm 0.71$
CDTG-2	12	-2.30 ± 0.29	$+0.92 \pm 0.57$	$+0.37 \pm 0.16$	$+0.72 \pm 0.71$	-0.23 ± 0.61	$+0.12 \pm 0.91$	$+0.46 \pm 0.42$
CDTG-3	11	-2.69 ± 0.35	$+1.40 \pm 0.89$	$+0.42 \pm 0.06$	$+0.13 \pm 0.35$	$+0.20 \pm \ldots$	$+0.62 \pm 1.48$	$+0.82 \pm 0.82$
CDTG-4	10	-2.22 ± 0.28	$+1.10 \pm 0.58$	$+0.31 \pm 0.15$	$+0.50 \pm 0.57$	$-0.20 \pm \ldots$	$+0.57 \pm 1.16$	$+0.86 \pm 0.76$
CDTG-5	10	-2.66 ± 0.57	$+0.94 \pm 0.43$	$+0.50 \pm 0.26$	$+0.50 \pm 0.63$	$+0.27 \pm \ldots$	-0.22 ± 1.00	$+0.34 \pm 0.48$
CDTG-6	10	-2.26 ± 0.32	$+1.07 \pm 0.59$	$+0.41 \pm 0.13$	-0.04 ± 0.74	$\ldots$	$+0.10 \pm 1.59$	$+0.66 \pm 0.56$
CDTG-7	9	-2.55 ± 0.37	$+0.80 \pm 0.16$	$+0.43 \pm 0.06$	$+0.51 \pm 0.31$	$\ldots$	$+1.06 \pm 1.04$	$+0.48 \pm 0.84$
CDTG-8	9	-2.27 ± 0.52	$+0.82 \pm 0.26$	$+0.34 \pm 0.14$	$+0.36 \pm 0.62$	$\ldots$	-0.04 ± 0.80	$+0.29 \pm 0.50$
CDTG-9	9	-2.66 ± 0.92	$+1.39 \pm 0.63$	$+0.44 \pm 0.30$	$+0.18 \pm 1.17$	$\ldots$	-0.16 ± 1.58	$+0.39 \pm 0.62$
CDTG-10	8	-2.51 ± 0.36	$+1.38 \pm 0.45$	$+0.51 \pm 0.23$	$+0.38 \pm \ldots$	$\ldots$	-0.18 ± 1.01	$+0.22 \pm 0.40$
CDTG-11	8	-2.20 ± 0.35	$+0.82 \pm 0.24$	$+0.48 \pm \ldots$	$+0.41 \pm 0.40$	-0.08 ± 0.01	$+0.29 \pm 0.76$	$+0.94 \pm 0.36$
CDTG-12	7	-2.71 ± 0.62	$+1.09 \pm 0.35$	$+0.55 \pm 0.11$	$+0.21 \pm 0.65$	$\ldots$	-0.13 ± 0.99	$+0.14 \pm 0.94$
CDTG-13	7	-1.95 ± 0.38	$+0.90 \pm 0.21$	$+0.69 \pm \ldots$	$+1.82 \pm 0.18$	$+0.99 \pm 0.95$	$+1.43 \pm 1.00$	$+1.19 \pm 0.34$
CDTG-14	7	-2.55 ± 0.81	$+1.33 \pm 0.60$	$+0.38 \pm 0.29$	$+0.10 \pm 0.53$	$-0.10 \pm \ldots$	$+1.36 \pm 1.38$	$+1.56 \pm \ldots$
CDTG-15	6	-3.50 ± 0.66	$+1.27 \pm 0.75$	$+0.47 \pm 0.07$	-0.56 ± 0.86	$\ldots$	$+0.02 \pm 1.31$	$+0.40 \pm 0.60$
CDTG-16	6	-2.51 ± 0.66	$+0.89 \pm 0.43$	$+0.43 \pm 0.08$	-0.08 ± 0.23	$\ldots$	$+0.08 \pm 0.53$	$+0.86 \pm 0.72$
CDTG-17	6	-2.21 ± 0.31	$+1.19 \pm 0.53$	$+0.46 \pm 0.09$	$+0.18 \pm 0.45$	$+0.17 \pm \ldots$	$+0.34 \pm 0.52$	$+0.39 \pm 0.19$
CDTG-18	6	-2.81 ± 0.71	$+1.34 \pm 0.42$	$+0.34 \pm 0.16$	$+0.33 \pm 1.09$	$\ldots$	-0.49 ± 0.77	$+0.79 \pm 0.23$
CDTG-19	5	-2.62 ± 0.77	$+1.23 \pm 0.55$	$+0.54 \pm 0.21$	$+0.39 \pm 0.72$	$\ldots$	$+0.11 \pm 1.06$	$+0.18 \pm 0.53$
CDTG-20	5	-2.44 ± 0.21	$+1.12 \pm 1.04$	$+0.34 \pm 0.11$	$+0.37 \pm 0.57$	$\ldots$	$+1.15 \pm 1.20$	$+0.48 \pm 0.12$
CDTG-21	5	-2.34 ± 0.08	$+1.36 \pm 0.37$	$+0.29 \pm 0.28$	-0.01 ± 1.40	$\ldots$	$+1.03 \pm 1.07$	$+0.40 \pm 0.43$
CDTG-22	5	-2.40 ± 0.57	$+0.78 \pm 0.07$	$+1.17 \pm \ldots$	$-0.18 \pm \ldots$	$+0.09 \pm 0.34$	-0.21 ± 1.02	$+0.88 \pm \ldots$
CDTG-23	5	-2.92 ± 0.71	$+0.78 \pm 0.10$	$+0.90 \pm 0.50$	-0.00 ± 0.79	$-0.15 \pm \ldots$	-0.34 ± 0.98	$+0.38 \pm \ldots$
CDTG-24	5	-1.89 ± 1.04	$+1.76 \pm 0.64$	$+0.80 \pm \ldots$	$+1.50 \pm 0.79$	$\ldots$	$+1.91 \pm 0.29$	$+1.11 \pm \ldots$
CDTG-25	4	-2.21 ± 0.34	$+1.65 \pm 0.70$	$+0.54 \pm \ldots$	$+1.16 \pm \ldots$	$-0.32 \pm \ldots$	$+0.58 \pm \ldots$	$+0.55 \pm \ldots$
CDTG-26	4	-2.55 ± 0.33	$+0.84 \pm 0.28$	$+0.53 \pm \ldots$	$-0.12 \pm \ldots$	$-0.20 \pm \ldots$	-0.50 ± 0.27	$-0.23 \pm \ldots$
CDTG-27	4	-2.80 ± 0.65	$+1.17 \pm 0.33$	$+0.38 \pm 0.24$	$+0.39 \pm 0.47$	$+1.73 \pm \ldots$	$+0.27 \pm 0.32$	$+0.94 \pm \ldots$
CDTG-28	4	-2.46 ± 0.54	$+0.90 \pm 0.21$	$+0.17 \pm \ldots$	$+0.83 \pm \ldots$	$+0.24 \pm 0.17$	$+0.37 \pm 0.16$	$+0.57 \pm \ldots$
CDTG-29	4	-2.39 ± 0.65	$+2.75 \pm 0.81$	$+0.30 \pm \ldots$	$+0.80 \pm 1.08$	$\ldots$	$+1.49 \pm 1.13$	$+1.39 \pm 0.71$
CDTG-30	4	-3.44 ± 0.52	$+2.16 \pm 1.60$	$+0.52 \pm 0.41$	$+0.67 \pm 1.41$	$\ldots$	$+0.69 \pm \ldots$	$+1.26 \pm \ldots$
CDTG-31	4	-2.86 ± 0.67	$+0.77 \pm 0.09$	$+0.31 \pm 0.25$	-0.22 ± 0.41	$\ldots$	-0.83 ± 0.64	$+0.90 \pm \ldots$
CDTG-32	4	-3.00 ± 1.09	$+1.88 \pm 0.41$	$+0.39 \pm 0.39$	$+0.07 \pm \ldots$	$\ldots$	$+1.02 \pm 0.71$	$+0.25 \pm \ldots$
CDTG-33	4	-2.63 ± 0.44	$+0.80 \pm 0.30$	$+0.50 \pm 0.05$	$+0.12 \pm 0.32$	$\ldots$	-0.41 ± 0.21	$+0.60 \pm 0.17$
CDTG-34	3	-2.62 ± 0.46	$+1.80 \pm 0.54$	$+0.44 \pm 0.17$	$+0.53 \pm \ldots$	$\ldots$	$+1.35 \pm 0.19$	$+0.55 \pm \ldots$
CDTG-35	3	-2.81 ± 0.41	$+1.32 \pm 0.60$	$+0.42 \pm \ldots$	$-0.42 \pm \ldots$	$+0.15 \pm \ldots$	$-0.39 \pm \ldots$	$+1.13 \pm \ldots$
CDTG-36	3	-2.27 ± 0.25	$+0.75 \pm 0.03$	$+0.59 \pm 0.34$	$+0.59 \pm 0.14$	$\ldots$	$+0.38 \pm 0.70$	$+0.72 \pm 0.13$
CDTG-37	3	-2.60 ± 0.04	$+1.05 \pm 0.16$	$\ldots$	$-0.01 \pm \ldots$	$-0.36 \pm \ldots$	-0.01 ± 0.01	$+0.50 \pm \ldots$
CDTG-38	3	-2.28 ± 0.20	$+1.35 \pm 0.79$	$+0.36 \pm \ldots$	$+0.33 \pm 0.27$	$\ldots$	$+0.33 \pm 0.68$	$+0.51 \pm 0.27$
CDTG-39	3	-2.86 ± 0.29	$+0.91 \pm 0.22$	$+0.27 \pm 0.08$	-0.42 ± 0.06	$\ldots$	-0.85 ± 0.67	-0.05 ± 0.47
CDTG-40	3	-2.20 ± 0.19	$+1.19 \pm 0.27$	$+0.23 \pm \ldots$	$+0.59 \pm \ldots$	$-0.21 \pm \ldots$	$+0.78 \pm 0.70$	$+0.86 \pm \ldots$
Biweight (CDTG mean):		-2.52 ± 0.05	$+1.12 \pm 0.05$	$+0.42 \pm 0.02$	$+0.27 \pm 0.07$	-0.03 ± 0.08	$+0.29 \pm 0.11$	$+0.60 \pm 0.06$
Biweight (CDTG std):		$+0.47 \pm 0.04$	$+0.43 \pm 0.04$	$\ldots$	$\ldots$	$\ldots$	$\ldots$	$\ldots$
IQR (CDTG mean):		**0.42**	**0.46**	**0.18**	**0.52**	**0.43**	**0.88**	**0.48**
IQR (CDTG std):		0.34	0.35	NaN	NaN	NaN	NaN	NaN
Biweight (Final):		-2.57 ± 0.59	$+1.13 \pm 0.63$	$+0.43 \pm 0.21$	$+0.17 \pm 0.71$	-0.06 ± 0.47	$+0.17 \pm 1.13$	$+0.51 \pm 0.65$
IQR (Final):		**0.80**	**0.97**	**0.26**	**0.86**	**0.47**	**1.62**	**0.80**

NOTE—The first section of the table lists the biweight location and scale of the abundances for each of the CDTGs. The second section of the table lists the mean and the standard error of the mean (using biweight estimates) for both the location and scale of the abundances of the CDTGs, along with the IQR of the abundances of the CDTGs. The third section of the table lists the biweight location and scale of the Final Sample for each of the abundances, along with the IQR for each of the abundances in the Final Sample.

5.3. *Results*

5.3.1. *The Full Sample of CEMP CDTGs*

Table 9 lists the means and dispersions of the elemental abundances explored in this study for each of the CDTGs identified in this work. The second part of the table lists the global CDTG properties, with the mean and standard error of the mean (using biweight location and scale) of both the CDTG means and dispersions being listed. The second part of the table also includes the IQR (Interquartile Range) of the CDTG means and dispersions. The third part of the table lists the biweight location and scale of the elemental abundances in the Final Sample, along with the IQR of the elemental abundances in the Final Sample. As can be seen by comparing the two IQRs for each the CDTG results and the Final Sample (indicated in bold face), the IQRs for the CDTG results for only 1 of the 7 el-

Table 10. CDTG Elemental-Abundance Statistics

Abundance	# CDTGs	$N < 0.50, 0.33, 0.25$	IEAD Probabilities	GEAD Probabilities	OEAD Probability
			All CDTGs		
[Fe/H]	40	20, 16, 15	56.3%, 21.7%, 5.4%	5.1%	0.3%
$[C/Fe]_c$	40	22, 16, 12	31.8%, 21.7%, 28.5%	12.9%	
[Mg/Fe]	28	13, 10, 6	71.4%, 44.9%, 73.6%	41.0%	
FEAD Probabilities			28.0%, 4.3%, 4.9%		
			Group I CDTGs		
[Fe/H]	16	8, 5, 5	59.8%, 65.0%, 37.0%	31.5%	12.0%
$[C/Fe]_c$	16	7, 2, 1	77.3%, 98.5%, 99.0%	76.9%	
[Mg/Fe]	7	4, 1, 0	50.0%, 93.9%, 100.0%	49.6%	
FEAD Probabilities			39.5%, 91.5%, 75.0%		
			Group II CDTGs		
[Fe/H]	9	5, 2, 1	47.8%, 85.2%, 92.5%	47.8%	< 0.1%
$[C/Fe]_c$	9	7, 7, 5	9.0%, 0.8%, 4.9%	0.6%	
[Mg/Fe]	5	3, 3, 3	50.0%, 20.5%, 10.4%	10.4%	
FEAD Probabilities			5.6%, 0.7%, 2.0%		

NOTE—The Individual Elemental-Abundance Dispersion (IEAD) probabilities represent the binomial probabilities for each element for the levels $v = 0.50$, 0.33, and 0.25, respectively. The Full Elemental-Abundance Dispersion (FEAD) probabilities represent the probabilities (across *all* elements) for the levels $v = 0.50$, 0.33, and 0.25, respectively. The Global Elemental-Abundance Dispersion (GEAD) probabilities represent the probabilities for the triplet of CDF levels for each element. The Overall Elemental-Abundance Dispersion (OEAD) probability represents the probability (across *all* elements) resulting from random draws from the full CDF.

ements considered is at least twice smaller ($[C/Fe]_c$), while the remaining 5 of the 7 elements have IQRs that narrowly miss the our rule of thumb, the exception being [Y/Fe], which has relatively few CDTGs with available dispersions. Going forward, we choose to only consider the statistical inferences that can be drawn by considering three elements, [Fe/H], $[C/Fe]_c$, and [Mg/Fe], and set the neutron-capture elements aside for our present analysis. We remind the reader that we are comparing how individual CDTGs dispersions compare to randomly generated clusters.

Table 10 lists the numbers of CDTGs with available estimates of the listed abundance ratios for [Fe/H], $[C/Fe]_c$, and [Mg/Fe], the numbers of CDTGs falling below the 0.50, 0.33, and 0.25 levels of the CDFs, and our calculated values for the various probabilities. Both the full and the overall probabilities (captured by the FEAD and the OEAD probability values) are statistically significant, indicating a similarity for all of the considered elements within our CDTGs across the entire sample (the only exception being the FEAD of $N < 0.5$). The individual abundance spreads (the GEAD probabilities), vary from marginal statistical significance for [Fe/H] to a lack of significance for $[C/Fe]_c$ and [Mg/Fe]. Keep in mind, as noted above, that the contrast in the mean IQRs of all three elements for our CDTGs with their can IQRs for the full sample may impact interpretation of their probabilities.

There are numerous lines of evidence that point towards Group I CEMP stars receiving their carbon enhancement from local events, for example accretion of material from a binary companion. This would clearly not affect the other stars in a given CDTG, and could vary a great deal even across the subset of CEMP Group I stars in an individual CDTG, given the ranges of mass possible for their erstwhile primary members, the initial separations of their members, and a host of other variables. To investigate this idea further, we proceed by separating the CEMP stars into their morphological groups, after removal of stars not assigned to groups, or which had ambiguous group assignments. We then carried out dynamical clustering within these subsets, and then performed the statistical analysis on each subset.

5.3.2. *The CEMP Group I and CEMP Group II Stars*

The CDTGs of CEMP Group I stars and CEMP Group II stars are listed in Table 13 and Table 16 of the Appendix, respectively. From inspection of Table 10, the FEAD and GEAD probabilities are substantially higher for the CDTGs of Group I CEMP stars than found for the Full Sample, and only the OEAD probability (12.0%) approaches marginal significance. However, for the Group II CEMP stars, the FEAD probabilities are either nearly significant (5.6% in the case of $N < 0.50$), or highly significant. The GEAD probability for [Fe/H] is not significant, while that for $[C/Fe]_c$ is

highly significant, and for [Mg/Fe] is marginally significant.

Inspection of Tables 15 and 18 in the Appendix underscore these differences. While the dispersions of the mean [Fe/H] for both the Group I and Group II CDTGs are essentially identical (0.30 dex and 0.21 dex, respectively), the contrast in the dispersions of the mean $[C/Fe]_c$ between the Group I and Group II CDTGs are quite clear (0.47 dex and 0.10 dex, respectively). Indeed, the *highest* $[C/Fe]_c$ dispersion of the Group II CDTGs is similar to the *mean* Group I CDTG $[C/Fe]_c$ dispersion.

Table 15 shows that the IQRs of the mean [Fe/H] and $[C/Fe]_c$ for the Group I CDTGs meets our factor of two rule of thumb compared to the parent population draws for these elements, while that for [Mg/Fe] (0.31 dex) is essentially identical to that for its parent population (0.26 dex). Table 18 shows that the IQRs of the Group II stars for [Fe/H], $[C/Fe]_c$, and [Mg/Fe] all satisfy our rule of thumb.

6. DISCUSSION AND FUTURE PERSPECTIVES

We now consider how to account for the observed behaviors of the CDTGs in our study, emphasizing the likely differences in the astrophysical origins of Group I (primarily CEMP-*s*) stars and Group II (primarily CEMP-no) stars.

Numerous studies support the binary mass-transfer scenario for the production of carbon for Group I stars. The work of Lucatello et al. (2005), Starkenburg et al. (2014), and Hansen et al. (2016a) showed that most CEMP-*s* stars are in fact member of binary systems, confirming results that apply to stars over a wide range of metallicities (e.g., Abate et al. 2013; Lee et al. 2014; Abate et al. 2015). Some have argued that this mechanism is responsible for the carbon enhancement in *all* CEMP stars. Hansen et al. (2016b) showed that Group II CEMP stars are not often associated with binary status. In contrast, Arentsen et al. (2019) suggested that they may be wide (long-period) binaries, and thus difficult to detect with a limited number of radial-velocity measurements. Suda et al. (2004) and Komiya et al. (2007, 2020) have argued that mass transfer from a long-period binary companion could explain the origin of the Group II CEMP stars. The recent work by Aguado et al. (2022) used carbon isotropic ratios to show that, for the mega metal-poor ([Fe/H] = −6.2)star SMSS 1605-1443, which we would classify as a Group III CEMP-no star, the carbon was *not* produced and transferred from an AGB binary companion.

There are also a variety of proposed mechanisms for producing carbon-enriched material for Group II stars in the early universe, including massive rapidly rotating stars and various SNe scenarios (Umeda & Nomoto 2003, 2005; Chieffi & Limongi 2004; Iwamoto et al. 2005; Meynet et al. 2006; Nomoto et al. 2006; Tominaga et al. 2007; Heger & Woosley 2010; Meynet et al. 2010; Limongi & Chieffi 2012; Ishigaki et al. 2014; Tominaga et al. 2014; Choplin et al. 2016; Salvadori et al. 2016; Kobayashi et al. 2020).

If the mass-transfer scenario applies to both Groups I and II CEMP CDTGs, they should both exhibit large dispersions in their corrected carbon-abundance distributions, as they would be due to local, and not global pollution events. A change in the abundances of a single star (or even multiple stars) in a CDTG would not affect the rest of the stars, leading to a wide dispersion in the elemental abundances. Based on our statistical analysis of the Group I and II CEMP dynamical clusters, this interpretation is unlikely, as they exhibit quite different behaviors. In particular, the small, and statistically significant, dispersion of the observed **corrected** carbon abundances within the Group II CDTGs points to the carbon coming from the environment that the stars formed in, rather than from enriched material transferred from binary companions. The dispersion in the mean $[C/Fe]_c$ for Group II CDTGs is already at the measurement limit for the observations, so it does not appear plausible to explain this low dispersion with anything but natal carbon abundances.

Note that the models described by Komiya et al. (2020) could produce carbon enhancements at low metallicity without considering a significant mass transfer, if some of their uncertain modeling parameters are considered. As they point out, the Fe yield of faint (mixing and fallback) supernovae is highly affected by the ejection factor, which controls the fraction of materials ejected from the region between the mass cut and the outer boundary of the mixing region. Also, [C/Fe] ratios could be affected by the diffusion coefficient, the amount of mass swept up by SNe, and the nature of the IMF. Their optimum model, with lower swept-up mass and diffusion coefficient could reproduce the trend of [C/Fe], while this model overproduces stars with [Fe/H] < -4 (Figure 14 of Komiya et al. 2020).

Taking into account these uncertainties, the contradiction between our results and the mass-transfer scenario might be mitigated. Komiya et al. (2020) only studied the effect of mass transfer in models without faint SNe. If they include mass transfer in models that include faint SNe, they would not need to assume a high rate of binary mass transfer to explain CEMP-no stars. In this case, the mass transfer, even if it occurs, may not significantly affect the low observed dispersion of carbon in Group II CDTGs.

Our results suggest the hypothesis that Group II CEMP stars are formed from the gas enriched by rapidly rotating massive stars or the ejecta of SNe with large carbon enhancements and depleted Fe production. Faint (mixing and fallback) SNe are one of the astrophysical candidates that have been suggested to be responsible (Umeda & Nomoto 2003, 2005; Iwamoto et al. 2005; Tominaga et al. 2007; Ishigaki et al. 2014). These SNe eject a small amount of Fe due to the large amount of fallback, resulting in ejecta with large [C/Fe] abundance ratios. Indeed, Tominaga et al. (2007) successfully reproduced the observed abundance pattern of the CEMP-no star CS 29498-043 (Aoki et al. 2004) with their 25 $M_{\odot}$ faint SN model. Thus, although the predicted [C/Fe] ratios are highly dependent on the choice of uncertain parameters, the ejecta from faint SNe could serve as one of the primary production sites for Group II CEMP stars.

Several studies have attempted to explain CEMP-no star formation solely from SNe ejecta (e.g., Salvadori et al. 2015; Sarmento et al. 2016; Chiaki et al. 2017; de Bennassuti et al. 2017; Sharma et al. 2018b,a; Hartwig & Yoshida 2019; Sarmento et al. 2019; Chiaki et al. 2020). Using the EAGLE cosmological hydrodynamical simulation (Schaye et al. 2015), Sharma et al. (2018b) found that low-metallicity core-collapse SNe with low Fe yields contribute to forming CEMP-no stars. Stars formed from such SNe exhibited high [C/Fe] and low [C/O], similar to CEMP-no stars' observed properties. Hartwig & Yoshida (2019) proposed a new scenario for forming CEMP-no stars. Their analytical estimates have shown that such stars could be formed from the carbon-rich material before those formed from carbon-normal gas in the inhomogeneous interstellar medium, due to the shorter cooling time of the carbon-enhanced gas. In this manner, CEMP-no stars could be formed from carbon-normal SNe.

Our results clearly favor one or more of the rapidly rotating massive-star and SNe scenarios, rather than the binary mass-transfer scenario(s). Note that, as shown in Table 10, the dispersion of [Mg/Fe] for the Group II CEMP stars is of marginal statistical significance, as reflected in the GEAD probability, unlike the highly significant behavior of $[C/Fe]_c$. While core-collapse SNe synthesize Mg, the lack of strong significance in [Mg/Fe] does not rule out this hypothesis for the stars in group Group II CDTGs, in part due to the limited number of Group II CDTGs (5) with measured [Mg/Fe] dispersions in our sample. Recent cosmological zoom-in simulations of MW-like galaxies show a low expected scatter of [Mg/Fe] in low-mass disrupted dwarf galaxies (Hirai et al. 2022), which would make detecting the similarities difficult.

Taking the available evidence as a whole, informed by the work in the current paper, we propose that most of the CEMP stars in Group II CDTGs (primarily CEMP-no stars) are formed from rapidly rotating, high-mass stars or the ejecta of various SNe, while stars in Group I CDTGs (primarily CEMP-s stars) are formed from binary mass transfer from an evolved companion. To confirm and refine these ideas, future studies need to explore the chemical nature of CDTGs with other elements, and conduct more comprehensive galaxy-formation simulations with improved modeling of CEMP star formation.

7. CONCLUSIONS

In this work, we have assembled a sample of CEMP stars with elemental abundances for a select number of species derived from moderate- to high-resolution spectroscopy. We then derived space velocities for the sample to estimate each star's dynamical parameters (E, J_r, J_ϕ, J_z) using `AGAMA`. Dynamical clustering of this sample using HDBSCAN resulted in the identification of 40 CDTGs. We found CDTGs to be associated with the following MW substructures: GSE, LMS-1, Thamnos, the Metal-Weak Thick Disk, the Splashed Disk and I'itoi. We only found a few CEMP CDTGs (4) to be associated with globular clusters, consistent with many previous claims of the lack of carbon-enhanced stars in these dense environments.

Finally, we separated the full sample of stars with available dynamical parameters into the CEMP morphological groups in the Yoon-Beers diagram of $A(C)_c$ vs. [Fe/H], and repeated the clustering exercise. Although the numbers of such clusters are reduced in total, the CEMP Group I CDTGs exhibit high $[C/Fe]_c$ dispersions, leading to the interpretation that the stars in these groups (primarily CEMP-s) likely arise from local enrichment events, such as mass transfer, in environments with extended star formation. In stark contrast, the CEMP Group II CDTGs exhibit such small dispersions in $[C/Fe]_c$ that we argue they cannot have arisen from local events, but formed instead from natal gas enriched by high-mass early generation rapidly rotating stars or SNe explosions in environments that did not support extended star formation, such as low-mass satellite galaxies.

We thank an anonymous referee for comments that helped clarify our presentation. J.Z., T.C.B., D.S., D.G., Y.H., J.Y., M.M., C.P., T.P., and S.C. acknowledge partial support for this work from grant PHY 14-30152; Physics Frontier Center/JINA Center for the Evolution of the Elements (JINA-CEE), and OISE-1927130: The International Research Network for Nuclear Astrophysics (IReNA), awarded by the US National Science Foundation. Y.H. is partly supported by JSPS KAKENHI Grant Numbers JP21J00153, JP20K14532, JP21H04499, JP21K03614, and JP22H01259. The work of V.M.P. is supported by NOIRLab, which is managed by the Association of Universities for Research in Astronomy (AURA) under a cooperative agreement with the National Science Foundation.

8. APPENDIX

Here we present the tables for the Initial Sample of CEMP stars (Table 11) and the Final Sample of CEMP stars (Table 12). In the print edition, only the table descriptions are provided; the full tables are available only in electronic form.

We show the results obtained for the Group I CDTGs (Table 13), their dynamical parameters (Table 14), and the means, dispersions, and Inter-Quartile Ranges of the CDTGs (Table 15). Similar tables for the Group II CDTGs are provided in Table 16, Table 17, and Table 18, respectively.

Table 11. Description of the Initial Sample of CEMP stars

Column	Field	Unit	Description
1	Name	–	The name of the star as given by the Reference
2	Source ID	–	The Gaia EDR3 Source ID of the star
3	RA	(J2000)	The Right Ascension of the star given in hours:minutes:seconds
4	DEC	(J2000)	The Declination of the star given in degrees:minutes:seconds
5	$V_{\rm mag}$	–	The V magnitude of the star as given by the $V_{\rm mag}$ Reference
6	$G_{\rm mag}$	–	The Gaia G mean magnitude of the star as given by the Gaia Source ID
7	$G_{\rm BP} - G_{\rm RP}$	–	The Gaia BP − RP color mean magnitude of the star as given by the Gaia Source ID
8	$V_{\rm mag}$ (Gaia)	–	The V magnitude of the star as determined by the transformations from G mag to V mag using $V = G + 0.02704 - 0.01424 * ({\rm BP} - {\rm RP}) + 0.2156 * ({\rm BP} - {\rm RP})^2 - 0.01426({\rm BP} - {\rm RP})^3$ given by Riello et al. (2021)
9	RV	(km s^{-1})	The radial velocity as given by RV Reference
10	Error	(km s^{-1})	The radial velocity error as given by RV Reference
11	$\rm RV_{Gaia}$	(km s^{-1})	The radial velocity as given by the Gaia Source ID
12	Error	(km s^{-1})	The radial velocity error as given by the Gaia Source ID
13	Parallax	(mas)	The parallax as given by the Gaia Source ID
14	Error	(mas)	The parallax error as given by the Gaia Source ID
15	Distance	(kpc)	The inverse parallax distance (1/Parallax)
16	Error	(kpc)	The inverse parallax distance error ($\rm Parallax_{error}/(Parallax^2)$)
19	Relative Error	–	The relative error of the corrected distance as given by Gaia
20	Distance BJ21	(kpc)	The 50 percentile distance as given by Bailer-Jones et al. (2021) based on the Gaia Source ID
21	Error	(kpc)	The 50 percentile error as estimated by the 84 percentile distance and the 16 percentile distance as given by Bailer-Jones et al. (2021) based on the Gaia Source ID ((dist84-dist16)/2)
22	Relative Error	–	The relative error of the 50 percentile distance as given by Bailer-Jones et al. (2021) based on the Gaia Source ID
23	Distance StarHorse	(kpc)	The 50 percentile distance as given by Anders et al. (2022) based on the Gaia Source ID
24	Error	(kpc)	The 50 percentile error as estimated by the 84 percentile distance and the 16 percentile distance as given by Anders et al. (2022) based on the Gaia Source ID ((dist84-dist16)/2)
25	Relative Error	–	The relative error of the 50 percentile distance as given by Anders et al. (2022) based on the Gaia Source ID
26	$\rm PM_{RA}$	(mas yr^{-1})	The proper motion in the Right Ascension as given by the Gaia Source ID
27	Error	(mas yr^{-1})	The proper motion error in the Right Ascension as given by the Gaia Source ID
28	$\rm PM_{DEC}$	(mas yr^{-1})	The proper motion in the Declination as given by the Gaia Source ID
29	Error	(mas yr^{-1})	The proper motion error in the Declination as given by the Gaia Source ID
30	Correlation Coefficient	–	The correlation coefficient between the proper motion in Right Ascension and the proper motion in Declination as given by the Gaia Source ID
31	$\rm T_{eff}$	(K)	The effective temperature of the star as given by the Reference
32	log g	(cgs)	The surface gravity of the star as given by the Reference
33	[Fe/H]	–	The metallicity of the star as given by (log ϵ(Fe) - log $\epsilon(\rm Fe)_\odot$) (Solar value of 7.5 taken from Asplund et al. (2009))
34	log ϵ(Fe)	–	The logarithmic iron abundance of the star as given by the Reference
35	[C/Fe]	–	The carbon abundance ratio of the star as given by (log ϵ(C) - log $\epsilon(\rm C)_\odot$ - [Fe/H]) (Solar value of 8.43 taken from Asplund et al. (2009))
36	log ϵ(C)	–	The logarithmic carbon abundance of the star as given by the Reference
37	$\rm [C/Fe]_c$	–	The carbon abundance ratio corrected for evolutionary effects from Placco et al. (2014)
38	$\rm AC_c$	–	The absolute carbon corrected for evolutionary effects from Placco et al. (2014) ($\rm [C/Fe]_c$

Table 11 *continued*

Table 11 *(continued)*

Column	Field	Unit	Description
			+ [Fe/H] + log $\epsilon(C)_\odot$) (Solar value of 8.43 taken from Asplund et al. (2009))
39	CARDET	–	Flag with "D" if the carbon abundance ratio ([C/Fe]) is detected by Reference and "U" if an upper limit by Reference and "L" if a lower limit by Reference and "X" if none is detected by Reference
40	[Mg/Fe]	–	The magnesium abundance ratio of the star as given by (log ϵ(Mg) - log $\epsilon(Mg)_\odot$ - [Fe/H]) (Solar value of 7.60 taken from Asplund et al. (2009))
41	log ϵ(Mg)	–	The logarithmic magnesium abundance of the star as given by the Reference
42	MAGDET	–	Flag with "D" if the magnesium abundance ratio ([Mg/Fe]) is detected by Reference and "U" if an upper limit by Reference and "L" if a lower limit by Reference and "X" if none is detected by Reference
43	[Sr/Fe]	–	The strontium abundance ratio of the star as given by (log ϵ(Sr) - log $\epsilon(Sr)_\odot$ - [Fe/H]) (Solar value of 2.87 taken from Asplund et al. (2009))
44	log ϵ(Sr)	–	The logarithmic strontium abundance of the star as given by the Reference
45	STRDET	–	Flag with "D" if the strontium abundance ratio ([Sr/Fe]) is detected by Reference and "U" if an upper limit by Reference and "L" if a lower limit by Reference and "X" if none is detected by Reference
46	[Y/Fe]	–	The yttrium abundance ratio of the star as given by (log ϵ(Y) - log $\epsilon(Y)_\odot$ - [Fe/H]) (Solar value of 2.21 taken from Asplund et al. (2009))
47	log ϵ(Y)	–	The logarithmic yttrium abundance of the star as given by the Reference
48	YTTDET	–	Flag with "D" if the yttrium abundance ratio ([Y/Fe]) is detected by Reference and "U" if an upper limit by Reference and "L" if a lower limit by Reference and "X" if none is detected by Reference
49	[Ba/Fe]	–	The barium abundance ratio of the star as given by (log ϵ(Ba) - log $\epsilon(Ba)_\odot$ - [Fe/H]) (Solar value of 2.18 taken from Asplund et al. (2009))
50	log ϵ(Ba)	–	The logarithmic barium abundance of the star as given by the Reference
51	BARDET	–	Flag with "D" if the barium abundance ratio ([Ba/Fe]) is detected by Reference and "U" if an upper limit by Reference and "L" if a lower limit by Reference and "X" if none is detected by Reference
52	[Eu/Fe]	–	The europium abundance ratio of the star as given by (log ϵ(Eu) - log $\epsilon(Eu)_\odot$ - [Fe/H]) (Solar value of 0.52 taken from Asplund et al. (2009))
53	log ϵ(Eu)	–	The logarithmic europium abundance of the star as given by the Reference
54	EURDET	–	Flag with "D" if the europium abundance ratio ([Eu/Fe]) is detected by Reference and "U" if an upper limit by Reference and "L" if a lower limit by Reference and "X" if none is detected by Reference
55	Class	–	The class for the star, as given by Table 1
56	Reference	–	The Reference for the star
57	$V_{\rm mag}$ Reference	–	The Reference for the V magnitude of the star
58	Distance AGAMA	–	The Reference for the distance used in AGAMA (StarHorse prioritized over BJ21 unless StarHorse distance has relative error greater than 0.3, if both have a relative error greater than 0.3 we adopt no distance estimate)

Table 12. Description of the Final Sample

Column	Field	Unit	Description
1	Name	–	The name of the star as given by the Reference
2	Source ID	–	The Gaia EDR3 Source ID of the star
3	RA	(J2000)	The Right Ascension of the star given in hours:minutes:seconds
4	DEC	(J2000)	The Declination of the star given in degrees:minutes:seconds
5	$V_{\rm mag}$	–	The V magnitude of the star as given by the $V_{\rm mag}$ Reference
6	$G_{\rm mag}$	–	The Gaia G mean magnitude of the star as given by the Gaia Source ID
7	$G_{\rm BP} - G_{\rm RP}$	–	The Gaia BP − RP color mean magnitude of the star as given by the Gaia Source ID
8	$V_{\rm mag}$ (Gaia)	–	The V magnitude of the star as determined by the transformations from G mag to V mag using $V = G + 0.02704 - 0.01424 * ({\rm BP} - {\rm RP}) + 0.2156 * ({\rm BP} - {\rm RP})^2 - 0.01426({\rm BP} - {\rm RP})^3$ given by Riello et al. (2021)
9	RV	(km s^{-1})	The radial velocity as given by RV Reference
10	Error	(km s^{-1})	The radial velocity error as given by RV Reference
11	$\rm RV_{Gaia}$	(km s^{-1})	The radial velocity as given by the Gaia Source ID
12	Error	(km s^{-1})	The radial velocity error as given by the Gaia Source ID
13	Parallax	(mas)	The parallax as given by the Gaia Source ID
14	Error	(mas)	The parallax error as given by the Gaia Source ID
15	Distance	(kpc)	The inverse parallax distance (1/Parallax)
16	Error	(kpc)	The inverse parallax distance error ($\rm Parallax_{error}/(Parallax^2)$)
17	Relative Error	–	The relative error of the corrected distance as given by Gaia
18	Distance BJ21	(kpc)	The 50 percentile distance as given by Bailer-Jones et al. (2021) based on the Gaia Source ID
19	Error	(kpc)	The 50 percentile error as estimated by the 84 percentile distance and the 16 percentile distance as given by Bailer-Jones et al. (2021) based on the Gaia Source ID ((dist84-dist16)/2)
20	Relative Error	–	The relative error of the 50 percentile distance as given by Bailer-Jones et al. (2021) based on the Gaia Source ID
21	Distance StarHorse	(kpc)	The 50 percentile distance as given by Anders et al. (2022) based on the Gaia Source ID
22	Error	(kpc)	The 50 percentile error as estimated by the 84 percentile distance and the 16 percentile distance as given by Anders et al. (2022) based on the Gaia Source ID ((dist84-dist16)/2)
23	Relative Error	–	The relative error of the 50 percentile distance as given by Anders et al. (2022) based on the Gaia Source ID
24	$\rm PM_{RA}$	(mas yr^{-1})	The proper motion in the Right Ascension as given by the Gaia Source ID
25	Error	(mas yr^{-1})	The proper motion error in the Right Ascension as given by the Gaia Source ID
26	$\rm PM_{DEC}$	(mas yr^{-1})	The proper motion in the Declination as given by the Gaia Source ID
27	Error	(mas yr^{-1})	The proper motion error in the Declination as given by the Gaia Source ID
28	Correlation Coefficient	–	The correlation coefficient between the proper motion in Right Ascension and the proper motion in Declination as given by the Gaia Source ID
29	$\rm T_{eff}$	(K)	The effective temperature of the star as given by the Reference
30	log g	(cgs)	The surface gravity of the star as given by the Reference
31	[Fe/H]	–	The metallicity of the star as given by (log ϵ(Fe) - log $\epsilon(\rm Fe)_\odot$) (Solar value of 7.5 taken from Asplund et al. (2009))
32	log ϵ(Fe)	–	The logarithmic iron abundance of the star as given by the Reference
33	[C/Fe]	–	The carbon abundance ratio of the star as given by (log ϵ(C) - log $\epsilon(\rm C)_\odot$ - [Fe/H]) (Solar value of 8.43 taken from Asplund et al. (2009))

Table 12 *continued*

Table 12 *(continued)*

Column	Field	Unit	Description
34	log ϵ(C)	–	The logarithmic carbon abundance of the star as given by the Reference
35	[C/Fe]$_c$	–	The carbon abundance ratio corrected for evolutionary effects from Placco et al. (2014)
36	AC$_c$	–	The absolute carbon corrected for evolutionary effects from Placco et al. (2014) ([C/Fe]$_c$ + [Fe/H] + log ϵ(C)$_\odot$) (Solar value of 8.43 taken from Asplund et al. (2009))
37	CARDET	–	Flag with "D" if the carbon abundance ratio ([C/Fe]) is detected by Reference and "U" if an upper limit by Reference and "L" if a lower limit by Reference and "X" if none is detected by Reference
38	[Mg/Fe]	–	The magnesium abundance ratio of the star as given by (log ϵ(Mg) - log ϵ(Mg)$_\odot$ - [Fe/H]) (Solar value of 7.60 taken from Asplund et al. (2009))
39	log ϵ(Mg)	–	The logarithmic magnesium abundance of the star as given by the Reference
40	MAGDET	–	Flag with "D" if the magnesium abundance ratio ([Mg/Fe]) is detected by Reference and "U" if an upper limit by Reference and "L" if a lower limit by Reference and "X" if none is detected by Reference
41	[Sr/Fe]	–	The strontium abundance ratio of the star as given by (log ϵ(Sr) - log ϵ(Sr)$_\odot$ - [Fe/H]) (Solar value of 2.87 taken from Asplund et al. (2009))
42	log ϵ(Sr)	–	The logarithmic strontium abundance of the star as given by the Reference
43	STRDET	–	Flag with "D" if the strontium abundance ratio ([Sr/Fe]) is detected by Reference and "U" if an upper limit by Reference and "L" if a lower limit by Reference and "X" if none is detected by Reference
44	[Y/Fe]	–	The yttrium abundance ratio of the star as given by (log ϵ(Y) - log ϵ(Y)$_\odot$ - [Fe/H]) (Solar value of 2.21 taken from Asplund et al. (2009))
45	log ϵ(Y)	–	The logarithmic yttrium abundance of the star as given by the Reference
46	YTTDET	–	Flag with "D" if the yttrium abundance ratio ([Y/Fe]) is detected by Reference and "U" if an upper limit by Reference and "L" if a lower limit by Reference and "X" if none is detectedby Reference
47	[Ba/Fe]	–	The barium abundance ratio of the star as given by (log ϵ(Ba) - log ϵ(Ba)$_\odot$ - [Fe/H]) (Solar value of 2.18 taken from Asplund et al. (2009))
48	log ϵ(Ba)	–	The logarithmic barium abundance of the star as given by the Reference
49	BARDET	–	Flag with "D" if the barium abundance ratio ([Ba/Fe]) is detected by Reference and "U" if an upper limit by Reference and "L" if a lower limit by Reference and "X" if none is detected by Reference
50	[Eu/Fe]	–	The europium abundance ratio of the star as given by (log ϵ(Eu) - log ϵ(Eu)$_\odot$ - [Fe/H]) (Solar value of 0.52 taken from Asplund et al. (2009))
51	log ϵ(Eu)	–	The logarithmic europium abundance of the star as given by the Reference
52	EURDET	–	Flag with "D" if the europium abundance ratio ([Eu/Fe]) is detected by Reference and "U" if an upper limit by Reference and "L" if a lower limit by Reference and "X" if none is detected by Reference
53	Class	–	The class for the star, as given by Table 1
54	Reference	–	The Reference for the star
55	$V_{\rm mag}$ Reference	–	The Reference for the V magnitude of the star
56	Distance AGAMA	–	The Reference for the distance used in AGAMA (StarHorse prioritized over BJ21 unless StarHorse distance has relative error greater than 0.3, if both have a relative error greater than 0.3 we adopt no distance estimate)
57	(v_r,v_ϕ,v_z)	(km s^{-1})	The cylindrical velocities of the star as given by AGAMA
58	Error	(km s^{-1})	The cylindrical velocity errors of the star as given by Monte Carlo sampling through AGAMA
59	(J_r,J_ϕ,J_z)	(kpc km s^{-1})	The cylindrical actions of the star as given by AGAMA
60	Error	(kpc km s^{-1})	The cylindrical action errors of the star as given by Monte Carlo sampling through AGAMA

Table 12 *continued*

Table 12 *(continued)*

Column	Field	Unit	Description
61	Energy	(km^2 s^{-2})	The orbital energy of the star as given by AGAMA
62	Error	(km^2 s^{-2})	The orbital energy error of the star as given by Monte Carlo sampling through AGAMA
63	r_{peri}	(kpc)	The Galactic pericentric distance of the star as given by AGAMA
64	Error	(kpc)	The Galactic pericentric distance error of the star as given by Monte Carlo sampling through AGAMA
65	r_{apo}	(kpc)	The Galactic apocentric distance of the star as given by AGAMA
66	Error	(kpc)	The Galactic apocentric distance error of the star as given by Monte Carlo sampling through AGAMA
67	Z_{max}	(kpc)	The maximum height above the Galactic plane of the star as given by AGAMA
68	Error	(kpc)	The maximum height above the Galactic plane error of the star as given by Monte Carlo sampling through AGAMA
69	Eccentricity	–	The eccentricity of the star given by $(r_{apo} - r_{peri})/(r_{apo} + r_{peri})$ through AGAMA
70	Error	–	The eccentricity error of the star as given by Monte Carlo sampling through AGAMA

Table 13. Group I CDTGs Identified by `HDBSCAN`

NAME	[Fe/H]	$[C/Fe]_c$	[Mg/Fe]	[Sr/Fe]	[Y/Fe]	[Ba/Fe]	[Eu/Fe]
CDTG−1−GI							
Structure: Unassigned Structure							
Group Assoc: Sequoia: Cordoni et al. (2021)							
Group Assoc: Fimbulthul: Malhan et al. (2022)							
Group Assoc: DTG-50: Shank et al. (2022b)							
Group Assoc: DTG-18: Shank et al. (2022a)							
Group Assoc: DTG-47: Shank et al. (2022a)							
Stellar Assoc: BS16543-97 (DTG-31: Limberg et al. 2021)							
Stellar Assoc: BPS BS 16543-0097 (DTC-16: Hattori et al. 2022)							
Stellar Assoc: CS22964-161 (DTG-31: Limberg et al. 2021)							
Stellar Assoc: CS22964-161 (DTG-31: Limberg et al. 2021)							
Globular Assoc: No Globular Associations							
Dwarf Galaxy Assoc: No Dwarf Galaxy Associations							
BPS CS 29497−0030	−2.52	+2.37	+0.35	+1.30	...	+2.75	+1.71
BPS BS 16543−0097	−2.48	+1.38	+0.66	+1.08	...	+0.43	+0.97
HE 1343−0640	−1.90	+0.73	+0.35	+0.78	...	+0.66	...
HE 1434−1442	−2.39	+2.09	+0.29	...	...	+1.19	...
Pristine J229.1219+00.9089	−2.25	+1.74	+0.16	+0.92	...	...	...
GALAH 170530003601365	−1.14	+0.92	...	+1.30	+1.02	+1.12	+0.29
BD+19 3109	−2.23	+2.51	...	...	...	+1.73	+0.72
BPS CS 22964−0161A	−2.37	+1.58	...	...	...	+1.36	...
BPS CS 22964−0161B	−2.39	+1.40	...	...	...	+1.30	...
BPS CS 22948−0027	−2.47	+2.58	+0.29	+0.95	...	+2.21	+1.87
BPS CS 22881−0036	−2.37	+1.99	+0.57	+1.06	...	+2.03	+0.58
$\boldsymbol{\mu \pm \sigma([X/Y])}$	$\mathbf{-2.37 \pm 0.15}$	$\mathbf{+1.77 \pm 0.64}$	$\mathbf{+0.33 \pm 0.18}$	$\mathbf{+1.05 \pm 0.19}$	$\mathbf{+1.02 \pm ...}$	$\mathbf{+1.44 \pm 0.71}$	$\mathbf{+0.96 \pm 0.64}$

NOTE—$\boldsymbol{\mu}$ and $\boldsymbol{\sigma}$ represent the biweight estimates of the location and scale for the abundances in the CDTG.

NOTE—This table is a stub; the full table is available in the electronic edition.

Table 14. Group I Cluster Dynamical Parameters Determined by `AGAMA`

Cluster	N Stars	$(\langle v_r\rangle,\langle v_\phi\rangle,\langle v_z\rangle)$	$(\langle J_r\rangle,\langle J_\phi\rangle,\langle J_z\rangle)$	$\langle E\rangle$	$\langle ecc\rangle$
		$(\sigma_{\langle v_r\rangle},\sigma_{\langle v_\phi\rangle},\sigma_{\langle v_z\rangle})$	$(\sigma_{\langle J_r\rangle},\sigma_{\langle J_\phi\rangle},\sigma_{\langle J_z\rangle})$	$\sigma_{\langle E\rangle}$	$\sigma_{\langle ecc\rangle}$
		(km s^{-1})	(kpc km s^{-1})	(10^5 km^2 s^{-2})	
CDTG−1−GI	11	(−22.4,−93.1,8.4)	(286.4,−634.0,84.8)	−1.805	0.61
		(86.1,32.4,56.4)	(132.1,197.4,26.6)	0.035	0.13
CDTG−2−GI	8	(9.9,155.4,12.4)	(184.6,1280.6,69.5)	−1.648	0.42
		(84.4,19.5,46.6)	(61.3,62.0,38.6)	0.029	0.07
CDTG−3−GI	7	(−17.9,82.1,−19.7)	(392.9,686.7,116.0)	−1.723	0.67
		(87.8,17.6,43.1)	(38.9,73.8,40.0)	0.026	0.03
CDTG−4−GI	6	(12.3,73.9,−133.1)	(197.1,648.9,563.0)	−1.630	0.47
		(34.3,1.6,13.3)	(50.1,92.5,116.6)	0.060	0.04
CDTG−5−GI	6	(−10.2,188.8,−8.9)	(31.8,1543.6,40.6)	−1.641	0.17
		(16.1,2.3,30.9)	(6.0,48.5,30.2)	0.027	0.02
CDTG−6−GI	6	(61.5,40.2,−25.7)	(417.0,221.0,1338.0)	−1.441	0.50
		(163.0,65.8,165.9)	(259.5,191.1,140.4)	0.063	0.13
CDTG−7−GI	5	(−56.6,−137.3,−129.6)	(168.9,−918.9,826.6)	−1.482	0.38
		(87.5,48.7,67.9)	(131.5,170.5,43.4)	0.006	0.14
CDTG−8−GI	5	(−16.0,45.8,30.6)	(448.1,373.5,96.8)	−1.799	0.78
		(77.7,4.8,43.2)	(23.3,85.5,20.6)	0.011	0.04
CDTG−9−GI	5	(−66.1,18.4,56.8)	(211.7,130.2,2001.7)	−1.308	0.32
		(127.8,38.2,291.2)	(257.9,327.0,30.3)	0.019	0.17
CDTG−10−GI	4	(−21.2,18.5,−97.6)	(828.2,121.9,233.3)	−1.597	0.94
		(178.8,5.7,84.8)	(62.9,32.2,24.8)	0.027	0.01
CDTG−11−GI	4	(−4.1,245.7,13.0)	(57.9,2028.9,42.9)	−1.496	0.20
		(55.3,18.4,29.1)	(6.7,76.8,31.0)	0.012	0.02
CDTG−12−GI	4	(−100.5,−21.6,81.1)	(1195.5,−244.1,683.1)	−1.338	0.89
		(128.5,0.7,137.7)	(94.2,170.4,72.5)	0.039	0.04
CDTG−13−GI	4	(−12.1,13.1,−67.9)	(491.5,96.7,232.5)	−1.789	0.92
		(52.3,12.6,38.1)	(23.2,93.2,23.1)	0.024	0.05
CDTG−14−GI	3	(−51.7,−27.2,−1.2)	(1234.7,−322.1,97.5)	−1.449	0.92
		(164.9,6.9,32.9)	(85.5,70.6,24.0)	0.038	0.02
CDTG−15−GI	3	(−8.3,63.5,−38.5)	(306.6,405.4,90.8)	−1.881	0.71
		(60.7,6.3,48.7)	(22.9,39.8,30.8)	0.020	0.05
CDTG−16−GI	3	(87.5,32.5,−11.8)	(614.9,299.5,204.5)	−1.669	0.86
		(26.3,14.0,84.7)	(18.2,155.8,13.2)	0.037	0.07

Table 15. Group I CDTG Abundance Means, Dispersions and Inter-Quartile Ranges (IQR)

Cluster	N Stars	[Fe/H]	$[C/Fe]_c$	[Mg/Fe]	[Sr/Fe]	[Y/Fe]	[Ba/Fe]	[Eu/Fe]
CDTG−1−GI	11	-2.37 ± 0.15	$+1.77 \pm 0.64$	$+0.33 \pm 0.18$	$+1.05 \pm 0.19$	$+1.02 \pm \ldots$	$+1.44 \pm 0.71$	$+0.96 \pm 0.64$
CDTG−2−GI	8	-2.16 ± 0.42	$+1.63 \pm 0.72$	$+0.39 \pm 0.25$	$+0.79 \pm 0.10$	$+1.54 \pm \ldots$	$+1.35 \pm 0.81$	$+1.29 \pm 0.84$
CDTG−3−GI	7	-2.29 ± 0.68	$+1.88 \pm 0.79$	$+0.31 \pm \ldots$	$+0.58 \pm 0.39$	$\ldots$	$+2.13 \pm 0.68$	$+1.44 \pm 0.71$
CDTG−4−GI	6	-2.39 ± 0.54	$+2.04 \pm 0.51$	$+0.29 \pm 0.16$	$+0.71 \pm 0.07$	$\ldots$	$+1.45 \pm 0.31$	$+1.30 \pm 0.36$
CDTG−5−GI	6	-1.86 ± 0.40	$+0.97 \pm 0.74$	$+0.69 \pm \ldots$	$+1.90 \pm \ldots$	$+1.66 \pm \ldots$	$+1.74 \pm 0.90$	$+1.34 \pm 0.20$
CDTG−6−GI	6	-2.10 ± 0.42	$+1.50 \pm 0.48$	$+0.38 \pm 0.17$	$+0.30 \pm 0.40$	$\ldots$	$+1.13 \pm 0.94$	$+0.94 \pm 0.72$
CDTG−7−GI	5	-2.96 ± 0.18	$+2.20 \pm 0.65$	$+0.40 \pm 0.13$	$+0.22 \pm 0.21$	$\ldots$	$+1.70 \pm 0.19$	$+0.92 \pm 0.45$
CDTG−8−GI	5	-2.26 ± 0.25	$+2.07 \pm 0.46$	$+0.28 \pm 0.24$	$+0.67 \pm 0.29$	$\ldots$	$+1.75 \pm 0.73$	$+1.31 \pm 0.74$
CDTG−9−GI	5	-2.12 ± 0.14	$+1.37 \pm 0.31$	$+0.19 \pm \ldots$	$+0.92 \pm 0.60$	$\ldots$	$+0.44 \pm 0.77$	$+0.72 \pm 0.20$
CDTG−10−GI	4	-2.49 ± 0.56	$+2.02 \pm 0.40$	$+0.34 \pm \ldots$	$+0.68 \pm \ldots$	$\ldots$	$+1.47 \pm 1.52$	$+1.56 \pm 0.30$
CDTG−11−GI	4	-1.58 ± 0.47	$+1.70 \pm 0.68$	$+0.80 \pm \ldots$	$+1.50 \pm 0.79$	$\ldots$	$+1.91 \pm 0.29$	$+1.11 \pm \ldots$
CDTG−12−GI	4	-2.35 ± 0.38	$+1.61 \pm 0.57$	$+0.63 \pm 0.34$	$+1.72 \pm \ldots$	$\ldots$	$+1.63 \pm 0.38$	$+0.68 \pm \ldots$
CDTG−13−GI	4	-2.24 ± 0.55	$+2.09 \pm 0.72$	$+0.64 \pm \ldots$	$+0.48 \pm 0.30$	$\ldots$	$+1.18 \pm 0.83$	$+1.37 \pm 0.38$
CDTG−14−GI	3	-2.47 ± 0.62	$+2.32 \pm 0.52$	$+0.36 \pm \ldots$	$+0.27 \pm \ldots$	$\ldots$	$+1.83 \pm \ldots$	$\ldots$
CDTG−15−GI	3	-2.44 ± 0.37	$+2.18 \pm 0.61$	$+0.63 \pm \ldots$	$+0.92 \pm 0.70$	$\ldots$	$+0.79 \pm 0.98$	$+0.68 \pm 0.22$
CDTG−16−GI	3	-2.50 ± 0.22	$+2.11 \pm 0.74$	$+0.37 \pm \ldots$	$+0.79 \pm \ldots$	$\ldots$	$+1.82 \pm 0.73$	$+0.34 \pm \ldots$
Biweight (CDTG mean):		-2.31 ± 0.07	$+1.90 \pm 0.09$	$+0.38 \pm 0.05$	$+0.72 \pm 0.12$	$+1.54 \pm 0.18$	$+1.56 \pm 0.10$	$+1.09 \pm 0.09$
Biweight (CDTG std):		$+0.40 \pm 0.04$	$+0.61 \pm 0.03$	$\ldots$	$\ldots$	$\ldots$	$\ldots$	$\ldots$
IQR (CDTG mean):		**0.30**	**0.47**	**0.31**	**0.40**	**0.32**	**0.46**	**0.51**
IQR (CDTG std):		0.30	0.22	$\ldots$	$\ldots$	$\ldots$	$\ldots$	$\ldots$
Biweight (Final):		-2.57 ± 0.59	$+1.13 \pm 0.63$	$+0.43 \pm 0.21$	$+0.17 \pm 0.71$	-0.06 ± 0.47	$+0.17 \pm 1.13$	$+0.51 \pm 0.65$
IQR (Final):		**0.80**	**0.97**	**0.26**	**0.86**	**0.47**	**1.62**	**0.80**

NOTE—The first section of the table lists the biweight location and scale of the abundances for each of the CDTGs. The second section of the table lists the mean and the standard error of the mean (using biweight estimates) for both the location and scale of the abundances of the CDTGs, along with the IQR of the abundances of the CDTGs. The third section of the table lists the biweight location and scale of the Final Sample for each of the abundances, along with the IQR for each of the abundances in the Final Sample.

Table 16. Group II CDTGs Identified by `HDBSCAN`

NAME	[Fe/H]	$[C/Fe]_c$	[Mg/Fe]	[Sr/Fe]	[Y/Fe]	[Ba/Fe]	[Eu/Fe]
CDTG−1−GII							
Structure: Unassigned Structure							
Group Assoc: C-3: Malhan et al. (2022)							
Group Assoc: NGC7089: Malhan et al. (2022)							
Group Assoc: DTG-9: Shank et al. (2022b)							
Group Assoc: DTG-110: Shank et al. (2022a)							
Group Assoc: DTG-117: Shank et al. (2022a)							
Stellar Assoc: HE 0420+0123a (DTC-3: Hattori et al. 2022)							
Stellar Assoc: J042314.50+013048.0 (DTG-99: Shank et al. 2022a)							
Stellar Assoc: J141640.80-242200.0 (DTG-43: Shank et al. 2022a)							
Stellar Assoc: J220216.40-053648.0 (DTG-110: Shank et al. 2022a)							
Globular Assoc: No Globular Associations							
Dwarf Galaxy Assoc: No Dwarf Galaxy Associations							
RAVE J030639.1−692040	−2.79	+0.79	...	−0.02	...	+0.20	−0.12
HE 0420+0123a	−3.03	+0.78	+0.44	+0.11	...	+0.08	+0.79
HE 1305−0331	−3.26	+1.09	...	−0.07	...	...	...
2MASS J14164084−2422000	−2.57	+0.87	+0.37	+0.02	...	−0.31	+0.14
SDSS J152953.94+080448.1	−3.18	+0.81	+0.22	...	...	−1.01	...
2MASS J19504989−3321107	−2.61	+0.70	−0.10	−0.35	...	−0.65	0.00
BPS CS 22873−0128	−3.24	+0.71	+0.59	−0.50	...	−1.45	−0.34
BPS CS 22956−0050	−3.57	+0.89	+0.57	−0.54	...	−1.00	−0.19
2MASS J22021636−0536483	−2.75	+0.75	...	+0.15	...	−0.75	−0.12
BPS CS 22886−0043	−2.40	+0.71	+0.55	+1.01	...	+0.54	+1.04
$\boldsymbol{\mu \pm \sigma([X/Y])}$	$\mathbf{-2.93 \pm 0.37}$	$\mathbf{+0.79 \pm 0.10}$	$\mathbf{+0.43 \pm 0.22}$	$\mathbf{-0.10 \pm 0.39}$	**...**	$\mathbf{-0.56 \pm 0.69}$	$\mathbf{-0.09 \pm 0.37}$

Note—$\boldsymbol{\mu}$ and $\boldsymbol{\sigma}$ represent the biweight estimates of the location and scale for the abundances in the CDTG.

Note—This table is a stub; the full table is available in the electronic edition.

Table 17. Group II Cluster Dynamical Parameters Determined by `AGAMA`

Cluster	N Stars	$(\langle v_r\rangle,\langle v_\phi\rangle,\langle v_z\rangle)$	$(\langle J_r\rangle,\langle J_\phi\rangle,\langle J_z\rangle)$	$\langle E\rangle$	$\langle ecc\rangle$
		$(\sigma_{\langle v_r\rangle},\sigma_{\langle v_\phi\rangle},\sigma_{\langle v_z\rangle})$	$(\sigma_{\langle J_r\rangle},\sigma_{\langle J_\phi\rangle},\sigma_{\langle J_z\rangle})$	$\sigma_{\langle E\rangle}$	$\sigma_{\langle ecc\rangle}$
		(km s^{-1})	(kpc km s^{-1})	(10^5 km^2 s^{-2})	
CDTG−1−GII	10	(−17.0,88.7,1.6)	(230.6,587.7,262.0)	−1.754	0.57
		(86.2,26.2,82.4)	(95.1,66.3,97.0)	0.069	0.09
CDTG−2−GII	8	(−60.2,−49.4,166.6)	(309.5,−323.5,641.9)	−1.691	0.61
		(84.6,36.8,28.4)	(69.3,242.8,37.9)	0.093	0.10
CDTG−3−GII	4	(−33.5,64.4,6.4)	(406.1,542.0,63.7)	−1.771	0.72
		(14.6,10.3,60.8)	(23.0,85.1,42.9)	0.020	0.04
CDTG−4−GII	4	(−20.8,44.9,−10.9)	(613.8,354.4,66.7)	−1.728	0.83
		(135.8,7.9,14.1)	(71.6,41.1,68.7)	0.021	0.01
CDTG−5−GII	4	(0.4,169.3,−45.9)	(76.3,1314.0,80.8)	−1.649	0.25
		(1.3,19.9,13.1)	(59.8,65.5,33.5)	0.009	0.11
CDTG−6−GII	3	(−25.3,19.5,−20.7)	(569.7,146.3,46.6)	−1.829	0.90
		(59.1,7.8,48.5)	(40.9,58.8,19.7)	0.012	0.06
CDTG−7−GII	3	(5.0,45.8,14.2)	(775.0,425.4,102.9)	−1.600	0.83
		(151.5,7.1,52.6)	(46.8,29.4,42.3)	0.044	0.02
CDTG−8−GII	3	(17.6,125.8,20.0)	(343.9,1182.7,66.3)	−1.595	0.53
		(97.2,4.2,39.8)	(40.6,114.6,47.9)	0.028	0.03
CDTG−9−GII	3	(−82.1,124.4,−83.6)	(396.7,610.2,902.0)	−1.475	0.55
		(85.6,40.8,109.0)	(94.2,185.1,52.5)	0.035	0.05

Table 18. Group II CDTG Abundance Means, Dispersions and Inter-Quartile Ranges (IQR)

Cluster	N Stars	[Fe/H]	$[C/Fe]_c$	[Mg/Fe]	[Sr/Fe]	[Y/Fe]	[Ba/Fe]	[Eu/Fe]
CDTG−1−GII	10	-2.93 ± 0.37	$+0.79 \pm 0.10$	$+0.43 \pm 0.22$	-0.10 ± 0.39	...	-0.56 ± 0.69	-0.09 ± 0.37
CDTG−2−GII	8	-3.23 ± 0.41	$+0.85 \pm 0.13$	$+0.50 \pm 0.10$	$+0.05 \pm 0.51$	$+0.20 \pm ...$	-0.76 ± 0.61	$+0.28 \pm 0.26$
CDTG−3−GII	4	-2.96 ± 0.21	$+0.91 \pm 0.19$	$+0.41 \pm 0.02$	-0.13 ± 0.42	...	-0.56 ± 0.30	$+1.10 \pm 0.37$
CDTG−4−GII	4	-3.17 ± 0.45	$+0.96 \pm 0.16$	$+0.29 \pm 0.07$	-0.22 ± 0.26	...	-1.32 ± 0.27	$+0.41 \pm 0.52$
CDTG−5−GII	4	-3.03 ± 0.19	$+0.91 \pm 0.22$	$+0.32 \pm ...$	-0.63 ± 0.60	...	-0.52 ± 0.26	$+0.29 \pm ...$
CDTG−6−GII	3	-2.85 ± 0.22	$+0.74 \pm 0.02$	$+0.44 \pm ...$	$-0.29 \pm ...$	...	$-0.49 \pm ...$	$+0.19 \pm 0.86$
CDTG−7−GII	3	-3.08 ± 0.45	$+0.84 \pm 0.07$	$+0.39 \pm ...$	$-0.23 \pm ...$	...	$-0.13 \pm ...$	$+1.79 \pm ...$
CDTG−8−GII	3	-3.35 ± 0.46	$+0.94 \pm 0.17$	$+0.58 \pm ...$	$-1.19 \pm ...$	...	-0.58 ± 0.76	$+0.17 \pm ...$
CDTG−9−GII	3	-3.15 ± 0.26	$+1.12 \pm 0.30$	$+0.64 \pm 0.17$	-0.41 ± 0.52	...	-0.45 ± 0.77	$+0.20 \pm 0.48$
Biweight (CDTG mean):		-3.08 ± 0.05	$+0.89 \pm 0.04$	$+0.44 \pm 0.04$	-0.23 ± 0.08	$+0.20 \pm 0.00$	-0.55 ± 0.04	$+0.23 \pm 0.07$
Biweight (CDTG std):		$+0.34 \pm 0.04$	$+0.15 \pm 0.03$	...	...	...	...	...
IQR (CDTG mean):		**0.21**	**0.10**	**0.11**	**0.28**	**0.00**	**0.09**	**0.22**
IQR (CDTG std):		0.23	0.09	...	...	...	...	...
Biweight (Final):		-2.57 ± 0.59	$+1.13 \pm 0.63$	$+0.43 \pm 0.21$	$+0.17 \pm 0.71$	-0.06 ± 0.47	$+0.17 \pm 1.13$	$+0.51 \pm 0.65$
IQR (Final):		**0.80**	**0.97**	**0.26**	**0.86**	**0.47**	**1.62**	**0.80**

Note—The first section of the table lists the biweight location and scale of the abundances for each of the CDTGs. The second section of the table lists the mean and the standard error of the mean (using biweight estimates) for both the location and scale of the abundances of the CDTGs, along with the IQR of the abundances of the CDTGs. The third section of the table lists the biweight location and scale of the Final Sample for each of the abundances, along with the IQR for each of the abundances in the Final Sample.

REFERENCES

Abate, C., Pols, O. R., Izzard, R. G., Mohamed, S. S., & de Mink, S. E. 2013, A&A, 552, A26, doi: 10.1051/0004-6361/201220007

Abate, C., Pols, O. R., Stancliffe, R. J., et al. 2015, A&A, 581, A62, doi: 10.1051/0004-6361/201526200

Abohalima, A., & Frebel, A. 2018, ApJS, 238, 36, doi: 10.3847/1538-4365/aadfe9

Aguado, D., Molaro, P., Caffau, E., et al. 2022, arXiv e-prints, arXiv:2210.04910. https://arxiv.org/abs/2210.04910

An, D., & Beers, T. C. 2020, ApJ, 897, 39, doi: 10.3847/1538-4357/ab8d39

Anders, F., Khalatyan, A., Queiroz, A. B. A., et al. 2022, A&A, 658, A91, doi: 10.1051/0004-6361/202142369

Aoki, W., Norris, J. E., Ryan, S. G., et al. 2004, ApJ, 608, 971, doi: 10.1086/420686

Arentsen, A., Starkenburg, E., Shetrone, M. D., et al. 2019, A&A, 621, A108, doi: 10.1051/0004-6361/201834146

Arentsen, A., Starkenburg, E., Aguado, D. S., et al. 2021, MNRAS, 505, 1239, doi: 10.1093/mnras/stab1343

Asplund, M., Grevesse, N., Sauval, A. J., & Scott, P. 2009, Annual Review of Astronomy & Astrophysics, 47, 481, doi: 10.1146/annurev.astro.46.060407.145222

Babusiaux, C., Fabricius, C., Khanna, S., et al. 2022, arXiv e-prints, arXiv:2206.05989. https://arxiv.org/abs/2206.05989

Bailer-Jones, C. A. L., Rybizki, J., Fouesneau, M., Demleitner, M., & Andrae, R. 2021, AJ, 161, 147, doi: 10.3847/1538-3881/abd806

Beers, T. C., & Christlieb, N. 2005, ARA&A, 43, 531, doi: 10.1146/annurev.astro.42.053102.134057

Beers, T. C., Flynn, K., & Gebhardt, K. 1990, AJ, 100, 32, doi: 10.1086/115487

Beers, T. C., Preston, G. W., & Shectman, S. A. 1985, AJ, 90, 2089, doi: 10.1086/113917

—. 1992, AJ, 103, 1987, doi: 10.1086/116207

Binney, J., & Tremaine, S. 2008, Galactic Dynamics: Second Edition (Princeton Series in Astrophysics)

Bisterzo, S., Gallino, R., Straniero, O., Cristallo, S., & Käppeler, F. 2011, MNRAS, 418, 284, doi: 10.1111/j.1365-2966.2011.19484.x

Bonaca, A., Conroy, C., Cargile, P. A., et al. 2020, ApJL, 897, L18, doi: 10.3847/2041-8213/ab9caa

Bonifacio, P., Caffau, E., Spite, M., et al. 2015, A&A, 579, A28, doi: 10.1051/0004-6361/201425266

Bromm, V., Coppi, P. S., & Larson, R. B. 1999, ApJL, 527, L5, doi: 10.1086/312385

Buder, S., Sharma, S., Kos, J., et al. 2021, Monthly Notices of the Royal Astronomical Society, 506, 150, doi: 10.1093/mnras/stab1242

Caffau, E., Bonifacio, P., François, P., et al. 2011, Nature, 477, 67, doi: 10.1038/nature10377

Campello, R. J. G. B., Moulavi, D., & Sander, J. 2013, in Advances in Knowledge Discovery and Data Mining, ed. J. Pei, V. S. Tseng, L. Cao, H. Motoda, & G. Xu (Berlin, Heidelberg: Springer Berlin Heidelberg), 160–172

Carollo, D., Freeman, K., Beers, T. C., et al. 2014, ApJ, 788, 180, doi: 10.1088/0004-637X/788/2/180

Carollo, D., Beers, T. C., Bovy, J., et al. 2012, ApJ, 744, 195, doi: 10.1088/0004-637X/744/2/195

Carollo, D., Chiba, M., Ishigaki, M., et al. 2019, ApJ, 887, 22, doi: 10.3847/1538-4357/ab517c

Cenarro, A. J., Moles, M., Cristóbal-Hornillos, D., et al. 2019, Astronomy & Astrophysics, 622, A176, doi: 10.1051/0004-6361/201833036

Chiaki, G., Tominaga, N., & Nozawa, T. 2017, MNRAS, 472, L115, doi: 10.1093/mnrasl/slx163

Chiaki, G., Wise, J. H., Marassi, S., et al. 2020, MNRAS, 497, 3149, doi: 10.1093/mnras/staa2144

Chieffi, A., & Limongi, M. 2004, ApJ, 608, 405, doi: 10.1086/392523

Choplin, A., Maeder, A., Meynet, G., & Chiappini, C. 2016, A&A, 593, A36, doi: 10.1051/0004-6361/201628083

Christlieb, N. 2003, Reviews in Modern Astronomy, 16, 191, doi: 10.1002/9783527617647.ch8

Cordoni, G., Da Costa, G. S., Yong, D., et al. 2021, MNRAS, 503, 2539, doi: 10.1093/mnras/staa3417

de Bennassuti, M., Salvadori, S., Schneider, R., Valiante, R., & Omukai, K. 2017, MNRAS, 465, 926, doi: 10.1093/mnras/stw2687

Deng, L.-C., Newberg, H. J., Liu, C., et al. 2012, Research in Astronomy and Astrophysics, 12, 735, doi: 10.1088/1674-4527/12/7/003

Dietz, S. E., Yoon, J., Beers, T. C., Placco, V. M., & Lee, Y. S. 2021, ApJ, 914, 100, doi: 10.3847/1538-4357/abefd6

Ezzeddine, R., Rasmussen, K., Frebel, A., et al. 2020, ApJ, 898, 150, doi: 10.3847/1538-4357/ab9d1a

Frebel, A. 2018, Annual Review of Nuclear and Particle Science, 68, 237, doi: 10.1146/annurev-nucl-101917-021141

Frebel, A., & Norris, J. E. 2015, ARA&A, 53, 631, doi: 10.1146/annurev-astro-082214-122423

Gaia Collaboration, Prusti, T., de Bruijne, J. H. J., et al. 2016, A&A, 595, A1, doi: 10.1051/0004-6361/201629272

Gaia Collaboration, Brown, A. G. A., Vallenari, A., et al. 2021, A&A, 649, A1, doi: 10.1051/0004-6361/202039657

Gravity Collaboration, Abuter, R., Amorim, A., et al. 2020, A&A, 636, L5, doi: 10.1051/0004-6361/202037813
Gudin, D., Shank, D., Beers, T. C., et al. 2021, ApJ, 908, 79, doi: 10.3847/1538-4357/abd7ed
Hansen, T., Hansen, C. J., Christlieb, N., et al. 2015, ApJ, 807, 173, doi: 10.1088/0004-637X/807/2/173
Hansen, T. T., Andersen, J., Nordström, B., et al. 2016a, A&A, 588, A3, doi: 10.1051/0004-6361/201527409
—. 2016b, A&A, 586, A160, doi: 10.1051/0004-6361/201527235
Hansen, T. T., Holmbeck, E. M., Beers, T. C., et al. 2018, ApJ, 858, 92, doi: 10.3847/1538-4357/aabacc
Hartwig, T., & Yoshida, N. 2019, ApJL, 870, L3, doi: 10.3847/2041-8213/aaf866
Hattori, K., Okuno, A., & Roederer, I. U. 2022, ApJ, Submitted, arXiv:2207.04110. https://arxiv.org/abs/2207.04110
Heger, A., & Woosley, S. E. 2010, ApJ, 724, 341, doi: 10.1088/0004-637X/724/1/341
Helmi, A. 2020, ARA&A, 58, 205, doi: 10.1146/annurev-astro-032620-021917
Helmi, A., & de Zeeuw, P. T. 2000, MNRAS, 319, 657, doi: 10.1046/j.1365-8711.2000.03895.x
Helmi, A., Veljanoski, J., Breddels, M. A., Tian, H., & Sales, L. V. 2017, A&A, 598, A58, doi: 10.1051/0004-6361/201629990
Herwig, F. 2005, ARA&A, 43, 435, doi: 10.1146/annurev.astro.43.072103.150600
Hirai, Y., Beers, T. C., Chiba, M., et al. 2022, MNRAS, in press, arXiv:2206.04060. https://arxiv.org/abs/2206.04060
Hirano, S., Hosokawa, T., Yoshida, N., Omukai, K., & Yorke, H. W. 2015, MNRAS, 448, 568, doi: 10.1093/mnras/stv044
Holmbeck, E. M., Hansen, T. T., Beers, T. C., et al. 2020, The Astrophysical Journal Supplement Series, 249, 30, doi: 10.3847/1538-4365/ab9c19
Ishigaki, M. N., Tominaga, N., Kobayashi, C., & Nomoto, K. 2014, ApJL, 792, L32, doi: 10.1088/2041-8205/792/2/L32
Iwamoto, N., Umeda, H., Tominaga, N., Nomoto, K., & Maeda, K. 2005, Science, 309, 451, doi: 10.1126/science.1112997
Keller, S. C., Schmidt, B. P., Bessell, M. S., et al. 2007, PASA, 24, 1, doi: 10.1071/AS07001
Kirby, E. N., Guo, M., Zhang, A. J., et al. 2015, ApJ, 801, 125, doi: 10.1088/0004-637X/801/2/125
Kobayashi, C., Karakas, A. I., & Lugaro, M. 2020, The Astrophysical Journal, 900, 179, doi: 10.3847/1538-4357/abae65
Komiya, Y., Suda, T., Minaguchi, H., et al. 2007, ApJ, 658, 367, doi: 10.1086/510826
Komiya, Y., Suda, T., Yamada, S., & Fujimoto, M. Y. 2020, ApJ, 890, 66, doi: 10.3847/1538-4357/ab67be
Kruijssen, J. M. D., Pfeffer, J. L., Chevance, M., et al. 2020, MNRAS, 498, 2472, doi: 10.1093/mnras/staa2452
Lee, Y. S., Beers, T. C., & Kim, Y. K. 2019, ApJ, 885, 102, doi: 10.3847/1538-4357/ab4791
Lee, Y. S., Beers, T. C., Kim, Y. K., et al. 2017, ApJ, 836, 91, doi: 10.3847/1538-4357/836/1/91
Lee, Y. S., Suda, T., Beers, T. C., & Stancliffe, R. J. 2014, ApJ, 788, 131, doi: 10.1088/0004-637X/788/2/131
Li, H., Du, C., Liu, S., Donlon, T., & Newberg, H. J. 2019, ApJ, 874, 74, doi: 10.3847/1538-4357/ab06f4
Li, H., Du, C., Yang, Y., et al. 2020, ApJ, 895, 23, doi: 10.3847/1538-4357/ab8733
Limberg, G., Rossi, S., Beers, T. C., et al. 2021, ApJ, 907, 10, doi: 10.3847/1538-4357/abcb87
Limongi, M., & Chieffi, A. 2012, ApJS, 199, 38, doi: 10.1088/0067-0049/199/2/38
Lövdal, S. S., Ruiz-Lara, T., Koppelman, H. H., et al. 2022, A&A, 665, A57, doi: 10.1051/0004-6361/202243060
Lucatello, S., Tsangarides, S., Beers, T. C., et al. 2005, ApJ, 625, 825, doi: 10.1086/428104
Lucchesi, R., Lardo, C., Jablonka, P., et al. 2022, MNRAS, doi: 10.1093/mnras/stab3721
Maeder, A., & Meynet, G. 2015, A&A, 580, A32, doi: 10.1051/0004-6361/201526234
Malhan, K., Ibata, R. A., Sharma, S., et al. 2022, ApJ, 926, 107, doi: 10.3847/1538-4357/ac4d2a
Mardini, M. K., Frebel, A., Chiti, A., et al. 2022, ApJ, 936, 78, doi: 10.3847/1538-4357/ac8102
McMillan, P. J. 2017, MNRAS, 465, 76, doi: 10.1093/mnras/stw2759
Mendes de Oliveira, C., Ribeiro, T., Schoenell, W., et al. 2019, Monthly Notices of the Royal Astronomical Society, 489, 241, doi: 10.1093/mnras/stz1985
Meynet, G., Ekström, S., & Maeder, A. 2006, A&A, 447, 623, doi: 10.1051/0004-6361:20053070
Meynet, G., Hirschi, R., Ekstrom, S., et al. 2010, A&A, 521, A30, doi: 10.1051/0004-6361/200913377
Monty, S., Venn, K. A., Lane, J. M. M., Lokhorst, D., & Yong, D. 2020, MNRAS, 497, 1236, doi: 10.1093/mnras/staa1995
Myeong, G. C., Evans, N. W., Belokurov, V., Koposov, S. E., & Sanders, J. L. 2017, MNRAS, 469, L78, doi: 10.1093/mnrasl/slx051
Myeong, G. C., Evans, N. W., Belokurov, V., Sanders, J. L., & Koposov, S. E. 2018, MNRAS, 478, 5449, doi: 10.1093/mnras/sty1403

Naidu, R. P., Conroy, C., Bonaca, A., et al. 2020, ApJ, 901, 48, doi: 10.3847/1538-4357/abaef4
—. 2022, ApJ, submitted, arXiv:2204.09057. https://arxiv.org/abs/2204.09057
Nomoto, K., Kobayashi, C., & Tominaga, N. 2013, ARA&A, 51, 457, doi: 10.1146/annurev-astro-082812-140956
Nomoto, K., Tominaga, N., Umeda, H., Kobayashi, C., & Maeda, K. 2006, Nuclear Physics A, 777, 424, doi: https://doi.org/10.1016/j.nuclphysa.2006.05.008
Omukai, K., Tsuribe, T., Schneider, R., & Ferrara, A. 2005, The Astrophysical Journal, 626, 627, doi: 10.1086/429955
Placco, V. M., Frebel, A., Beers, T. C., & Stancliffe, R. J. 2014, ApJ, 797, 21, doi: 10.1088/0004-637X/797/1/21
Rasmussen, K. C., Zepeda, J., Beers, T. C., et al. 2020, The Astrophysical Journal, 905, 20, doi: 10.3847/1538-4357/abc005
Reid, M. J., & Brunthaler, A. 2020, ApJ, 892, 39, doi: 10.3847/1538-4357/ab76cd
Riello, M., De Angeli, F., Evans, D. W., et al. 2021, Astronomy & Astrophysics, 649, A3, doi: 10.1051/0004-6361/202039587
Rockosi, C. M., Lee, Y. S., Morrison, H. L., et al. 2022, ApJS, 259, 60, doi: 10.3847/1538-4365/ac5323
Roederer, I. U., Hattori, K., & Valluri, M. 2018, AJ, 156, 179, doi: 10.3847/1538-3881/aadd9c
Rossi, S., Beers, T. C., Sneden, C., et al. 2005, The Astronomical Journal, 130, 2804, doi: 10.1086/497164
Sakari, C. M., Placco, V. M., Farrell, E. M., et al. 2018, The Astrophysical Journal, 868, 110, doi: 10.3847/1538-4357/aae9df
Salvadori, S., Skúladóttir, Á., & de Bennassuti, M. 2016, Astronomische Nachrichten, 337, 935, doi: 10.1002/asna.201612402
Salvadori, S., Skúladóttir, Á., & Tolstoy, E. 2015, MNRAS, 454, 1320, doi: 10.1093/mnras/stv1969
Sarmento, R., Scannapieco, E., & Côté, B. 2019, ApJ, 871, 206, doi: 10.3847/1538-4357/aafa1a
Sarmento, R., Scannapieco, E., & Pan, L. 2016, The Astrophysical Journal, 834, 23, doi: 10.3847/1538-4357/834/1/23
Schaye, J., Crain, R. A., Bower, R. G., et al. 2015, MNRAS, 446, 521, doi: 10.1093/mnras/stu2058
Schlafly, E. F., & Finkbeiner, D. P. 2011, ApJ, 737, 103, doi: 10.1088/0004-637X/737/2/103
Schlegel, D. J., Finkbeiner, D. P., & Davis, M. 1998, ApJ, 500, 525, doi: 10.1086/305772
Schönrich, R., Binney, J., & Dehnen, W. 2010, MNRAS, 403, 1829, doi: 10.1111/j.1365-2966.2010.16253.x
Sestito, F., Longeard, N., Martin, N. F., et al. 2019, MNRAS, 484, 2166, doi: 10.1093/mnras/stz043
Shank, D., Komater, D., Beers, T. C., Placco, V. M., & Huang, Y. 2022, The Astrophysical Journal Supplement Series, 261, 19, doi: 10.3847/1538-4365/ac680c
Shank, D., Beers, T. C., Placco, V. M., et al. 2022a, ApJ, Submitted, arXiv:2208.09712. https://arxiv.org/abs/2208.09712
—. 2022b, ApJ, 926, 26, doi: 10.3847/1538-4357/ac409a
Sharma, M., Theuns, T., & Frenk, C. 2018a, MNRAS, 479, 1638, doi: 10.1093/mnras/sty1319
Sharma, M., Theuns, T., Frenk, C. S., & Cooke, R. J. 2018b, MNRAS, 473, 984, doi: 10.1093/mnras/stx2392
Spite, M., Caffau, E., Bonifacio, P., et al. 2013, A&A, 552, A107, doi: 10.1051/0004-6361/201220989
Stancliffe, R. J., Glebbeek, E., Izzard, R. G., & Pols, O. R. 2007, A&A, 464, L57, doi: 10.1051/0004-6361:20066891
Starkenburg, E., Shetrone, M. D., McConnachie, A. W., & Venn, K. A. 2014, MNRAS, 441, 1217, doi: 10.1093/mnras/stu623
Starkenburg, E., Martin, N., Youakim, K., et al. 2017, Monthly Notices of the Royal Astronomical Society, 471, 2587, doi: 10.1093/mnras/stx1068
Suda, T., Aikawa, M., Machida, M. N., Fujimoto, M. Y., & Icko Iben, J. 2004, The Astrophysical Journal, 611, 476, doi: 10.1086/422135
Suda, T., Katsuta, Y., Yamada, S., et al. 2008, PASJ, 60, 1159, doi: 10.1093/pasj/60.5.1159
Tominaga, N., Iwamoto, N., & Nomoto, K. 2014, The Astrophysical Journal, 785, 98, doi: 10.1088/0004-637x/785/2/98
Tominaga, N., Umeda, H., & Nomoto, K. 2007, ApJ, 660, 516, doi: 10.1086/513063
Umeda, H., & Nomoto, K. 2003, Nature, 422, 871, doi: 10.1038/nature01571
—. 2005, ApJ, 619, 427, doi: 10.1086/426097
Vasiliev, E. 2018, Monthly Notices of the Royal Astronomical Society, 482, 1525, doi: 10.1093/mnras/sty2672
Vasiliev, E., & Baumgardt, H. 2021, MNRAS, 505, 5978, doi: 10.1093/mnras/stab1475
Whitten, D. D., Placco, V. M., Beers, T. C., et al. 2019, A&A, 622, A182, doi: 10.1051/0004-6361/201833368
—. 2021, ApJ, 912, 147, doi: 10.3847/1538-4357/abee7e
Yanny, B., Rockosi, C., Newberg, H. J., et al. 2009, AJ, 137, 4377, doi: 10.1088/0004-6256/137/5/4377
Yoon, J., Beers, T. C., Placco, V. M., et al. 2016, ApJ, 833, 20, doi: 10.3847/0004-637X/833/1/20

Yoon, J., Beers, T. C., Dietz, S., et al. 2018, The Astrophysical Journal, 861, 146, doi: 10.3847/1538-4357/aaccea

York, D. G., Adelman, J., Anderson, John E., J., et al. 2000, AJ, 120, 1579, doi: 10.1086/301513

Yuan, Z., Chang, J., Beers, T. C., & Huang, Y. 2020, ApJL, 898, L37, doi: 10.3847/2041-8213/aba49f

Yuan, Z., Myeong, G. C., Beers, T. C., et al. 2020, The Astrophysical Journal, 891, 39, doi: 10.3847/1538-4357/ab6ef7

Zepeda, J., Rasmussen, K. C., Beers, T. C., et al. 2022, ApJ, 927, 13, doi: 10.3847/1538-4357/ac3a79